Cluster Difference Imaging Photometric Survey. II. TOI 837: A Young Validated Planet in IC 2602

L. G. Bouma,[1] J. D. Hartman,[1] R. Brahm,[2,3] P. Evans,[4] K. A. Collins,[5] G. Zhou,[5] P. Sarkis,[6] S. N. Quinn,[5] J. de Leon,[7]
J. Livingston,[7] C. Bergmann,[8,9] K. G. Stassun,[10,11] W. Bhatti,[1] J. N. Winn,[1] G. Á. Bakos,[1] L. Abe,[12] N. Crouzet,[13]
G. Dransfield,[14] W. Marie-Sainte,[15] D. Mékarnia,[12] A. H.M.J. Triaud,[14] C. G. Tinney,[8] T. Henning,[6] N. Espinoza,[16]
A. Jordán,[2,3] M. Barbieri,[17] S. Nandakumar,[17] T. Trifonov,[6] J. I. Vines,[18] M. Vuckovic,[19] C. Ziegler,[20] N. Law,[21]
A. W. Mann,[21] G. R. Ricker,[22] R. Vanderspek,[22] S. Seager,[23] J. M. Jenkins,[24] C. J. Burke,[22] D. Dragomir,[25]
A. M. Levine,[22] E. V. Quintana,[26] J. E. Rodriguez,[5] J. C. Smith,[24,27] and B. Wohler[24,27]

[1]*Department of Astrophysical Sciences, Princeton University, 4 Ivy Lane, Princeton, NJ 08540, USA*

[2]*Facultad de Ingeniería y Ciencias, Universidad Adolfo Ibáñez, Av. Diagonal las Torres 2640, Peñalolén, Santiago, Chile*

[3]*Millennium Institute for Astrophysics, Chile*

[4]*El Sauce Observatory, Coquimbo Province, Chile*

[5]*Center for Astrophysics | Harvard & Smithsonian, 60 Garden St, Cambridge, MA 02138, USA*

[6]*Max-Planck-Institut für Astronomie, Königstuhl 17, Heidelberg 69117, Germany*

[7]*Department of Astronomy, University of Tokyo, 7-3-1 Hongo, Bunkyo-ky, Tokyo 113-0033, Japan*

[8]*Exoplanetary Science at UNSW, School of Physics, UNSW Sydney, NSW 2052, Australia*

[9]*Deutsches Zentrum für Luft- und Raumfahrt, Münchener Str. 20, 82234 Wessling, Germany*

[10]*Vanderbilt University, Department of Physics & Astronomy, 6301 Stevenson Center Lane, Nashville, TN 37235, USA*

[11]*Fisk University, Department of Physics, 1000 17th Avenue N., Nashville, TN 37208, USA*

[12]*Université Côte d'Azur, Observatoire de la Côte d'Azur, CNRS, Laboratoire Lagrange, Bd de l'Observatoire, CS 34229, 06304 Nice cedex 4, France*

[13]*European Space Agency, European Space Research and Technology Centre (ESA/ESTEC), Keplerlaan 1, 2201 AZ Noordwijk, The Netherlands*

[14]*School of Physics & Astronomy, University of Birmingham, Edgbaston, Birmingham B15 2TT, United Kingdom*

[15]*Institut Paul Émile Victor, Concordia Station, Antarctica*

[16]*Space Telescope Science Institute, 3700 San Martin Drive, Baltimore, MD 21218, USA*

[17]*INCT, Universidad de Atacama, calle Copayapu 485, Copiapó, Atacama, Chile*

[18]*Departamento de Astronomía, Universidad de Chile, Camino El Observatorio 1515, Las Condes, Santiago, Chile*

[19]*Instituto de Física y Astronomía, Universidad de Vaparaíso, Casilla 5030, Valparaíso, Chile*

[20]*Dunlap Institute for Astronomy and Astrophysics, University of Toronto, 50 St. George Street, Toronto, Ontario M5S 3H4, Canada*

[21]*Department of Physics and Astronomy, The University of North Carolina at Chapel Hill, Chapel Hill, NC 27599-3255, USA*

[22]*Department of Physics and Kavli Institute for Astrophysics and Space Research, Massachusetts Institute of Technology, Cambridge, MA 02139, USA*

[23]*Department of Earth, Atmospheric, and Planetary Sciences, Massachusetts Institute of Technology, Cambridge, MA 02139, USA*

[24]*NASA Ames Research Center, Moffett Field, CA 94035, USA*

[25]*Department of Physics and Astronomy, University of New Mexico, Albuquerque, NM, USA*

[26]*NASA Goddard Space Flight Center, 8800 Greenbelt Road, Greenbelt, MD 20771, USA*

[27]*SETI Institute, Mountain View, CA 94043, USA*

ABSTRACT

We report the discovery of TOI 837b and its validation as a transiting planet. We characterize the system using data from the NASA TESS mission, the ESA Gaia mission, ground-based photometry from El Sauce and ASTEP400, and spectroscopy from CHIRON, FEROS, and Veloce. We find that TOI 837 is a $T = 9.9$ mag G0/F9 dwarf in the southern open cluster IC 2602. The star and planet are therefore 35^{+11}_{-5} million years old. Combining the transit photometry with a prior on the stellar parameters derived from the cluster color-magnitude diagram, we find that the planet has an orbital period of 8.3 d and is slightly smaller than Jupiter ($R_p = 0.77^{+0.09}_{-0.07} R_{\rm Jup}$). From radial velocity monitoring, we limit $M_p \sin i$ to less than 1.20 $M_{\rm Jup}$ (3-σ). The transits either graze or nearly graze the stellar limb. Grazing transits are a cause for concern, as they are often indicative of

Corresponding author: L. G. Bouma
luke@astro.princeton.edu

astrophysical false positive scenarios. Our follow-up data show that such scenarios are unlikely. Our combined multi-color photometry, high-resolution imaging, and radial velocities rule out hierarchical eclipsing binary scenarios. Background eclipsing binary scenarios, though limited by speckle imaging, remain a 0.2% possibility. TOI 837b is therefore a validated adolescent exoplanet. The planetary nature of the system can be confirmed or refuted through observations of the stellar obliquity and the planetary mass. Such observations may also improve our understanding of how the physical and orbital properties of exoplanets change in time.

1. INTRODUCTION

Over the first 100 million years of their lives, exoplanet systems are expected to undergo major physical and dynamical changes. For a typical Sun-like star, the protoplanetary disk disperses within roughly 1–10 million years (Mamajek 2009; Fedele et al. 2010; Dullemond & Monnier 2010; Williams & Cieza 2011). Gas giants presumably finish accreting before the end of disk dispersal (Pollack et al. 1996). While rocky planets may form within only a few million years (Dauphas & Pourmand 2011), they can also undergo significant growth over the next 10–100 million years through giant impacts (*e.g.*, Kleine et al. 2009; König et al. 2011; Morbidelli et al. 2012; Raymond et al. 2014). The Moon, for instance, may have formed from debris ejected during a collision between the proto-Earth and a planetesimal during Earth's first 100 million years (Cameron & Ward 1976; Canup & Asphaug 2001; Touboul et al. 2007).

A number of other processes are expected to shape young exoplanets. After accreting, planets with gaseous envelopes are thought to cool and contract, and their atmospheres are expected to undergo a mix of photoevaporation and core-powered mass loss (*e.g.*, Fortney et al. 2007; Owen & Wu 2013; Fulton et al. 2017; Gupta & Schlichting 2019, 2020). Predicted timescales for photoevaporation and core-powered mass loss range from 10 million years to over 1 gigayear for typical transiting sub-Neptunes (Ginzburg et al. 2016; Owen & Wu 2017; King & Wheatley 2020). The relative importance of each process is set by the planetary surface gravity and the radiation environment. Both processes can be directly observed in favorable cases using the metastable 1083 nm He line (Spake et al. 2018; Oklopčić & Hirata 2018; Mansfield et al. 2018).

Beyond physical changes, dynamical changes are expected in the semi-major axes, eccentricities, and stellar obliquities of young planets. When the gas disk is present, the planetary semi-major axis is thought to change in step with the viscous evolution of the disk (Lin et al. 1996). High-eccentricity migration processes including planet-planet scattering, secular chaos, and Kozai-Lidov oscillations can also occur (*e.g.*, Fabrycky & Tremaine 2007; Chatterjee et al. 2008; Lithwick & Wu 2014). The circularization timescale is thought to be such that for any giant planets that do migrate early, their orbits should circularize within 100 million years (Zahn 1977; Bonomo et al. 2017).

Finding and understanding systems undergoing these evolutionary changes is a major goal in contemporary exoplanet research. To identify stars younger than say 1 gigayear, a number of direct and indirect methods are available (Soderblom 2010). The traditional approach is to isochronally age-date coeval groups of stars, hereafter "clusters" (*e.g.*, Lada & Lada 2003; Zuckerman & Song 2004; Krumholz et al. 2019). Young field stars can also be identified isochronally, provided that they are sufficiently massive (Berger et al. 2020). Other age indicators include stellar rotation periods, the abundance of photospheric lithium, and chromospheric diagnostics such as calcium emission and broadband UV emission. Studies by, for instance, Sanchis-Ojeda et al. (2013), David et al. (2018), and G. Zhou et al. (2020, submitted) have combined these methods to age-date individual field stars hosting transiting planets. Many of these latter methods were summarized by Mamajek & Hillenbrand (2008), and have since been calibrated by, *e.g.*, Irwin & Bouvier (2009); Barnes et al. (2015); Meibom et al. (2015); Angus et al. (2015) and Curtis et al. (2019b) for stellar rotation, Žerjal et al. (2017) for chromospheric activity, and *e.g.*, Berger et al. (2018) and Žerjal et al. (2019) for lithium abundances.

To date, a few dozen planets in clusters have been detected, and fewer still have been closely characterized. Despite the challenges of starspot-induced radial velocity (RV) variations, RV surveys found early success in the Hyades, NGC 2423, Praesepe, and M 67 (Sato et al. 2007; Lovis & Mayor 2007; Quinn et al. 2012; Malavolta et al. 2016; Brucalassi et al. 2017). RV surveys of highly active pre-main sequence stars in Taurus also led to the youngest hot Jupiters yet reported orbiting V830 Tau, TAP 26, and CI Tau (Donati et al. 2016; Johns-Krull et al. 2016; Yu et al. 2017; Biddle et al. 2018; Flagg et al. 2019). The planetary nature of at least two of these signals has been debated (Donati et al. 2020; Damasso et al. 2020).

The transit method was comparatively slow to catch up. Early deep transit searches of open clusters by many groups did not yield definitive planet detections (Mochejska et al. 2005, 2006; Burke et al. 2006; Aigrain et al. 2007; Irwin et al. 2007; Miller et al. 2008; Pepper et al. 2008; Hartman et al. 2009). These searches were typically sensitive to planets larger than Jupiter, on $\lesssim 3$ day orbital periods. Hot Jupiter occurrence rate limits were derived at the $\lesssim 5\%$ level (*e.g.*, Burke et al. 2006; Hartman et al. 2009). The modern 0.5-1% occurrence rate suggests that these early transit surveys would have needed a greater data volume at higher precision

for detection to be possible (Mayor et al. 2011; Wright et al. 2012; Howard et al. 2012; Petigura et al. 2018).

Kepler observed a large enough number of stars with sufficient baseline and precision to detect transiting planets in open clusters: Kepler-66b and 67b, in the gigayear-old NGC 6811 (Borucki et al. 2010; Meibom et al. 2013). Though a broken reaction wheel ended the prime Kepler mission, the repurposed K2 (Howell et al. 2014) switched between fields along the ecliptic every quarter-year, and was able to observe far more clusters and young stars.

The discoveries made by K2 through its surveys of Taurus, the Hyades, Praesepe, and Upper Sco were a major inspiration for the present work (*e.g.*, Mann et al. 2016a; Obermeier et al. 2016; Mann et al. 2017; Vanderburg et al. 2018; Ciardi et al. 2018; Livingston et al. 2018; Mann et al. 2018; Rizzuto et al. 2018; Livingston et al. 2019). Observations with K2 convincingly showed that at least some close-in planets must form within about 10 Myr (Mann et al. 2016b; David et al. 2016). They also led to the first hints that young planets in clusters may in fact be qualitatively different from their field counterparts. For instance, based on its observed mass, radius, and UV environment, the 700 Myr K2-100b is probably actively losing its atmosphere, and should become a bare rocky planet over the next few hundred Myr (Mann et al. 2017; Barragán et al. 2019). The four transiting planets around V1298 Tau (23 Myr) are also likely to be photoevaporating, and could represent a precursor to Kepler's compact multiple systems (David et al. 2019a,b).

To advance the young planet census, we have been using data from the TESS spacecraft (Ricker et al. 2015) to perform a Cluster Difference Imaging Photometric Survey (CDIPS; Bouma et al. 2019). Our targets in this survey are candidate young stars that have been reported in the literature. At the time of writing, $\sim 6 \times 10^5$ light curves from Year 1 of TESS had been created and were available through MAST[1], and via DOI.ORG/10.17909/T9-AYD0-K727. Searching through a subset of these light curves brought our attention to the candidate transiting planet, TOI 837b, that is the subject of this analysis.

The transits of TOI 837b are grazing the stellar limb, which is a cause for concern. Particularly for a star near the galactic plane ($b = -5.8°$), background eclipsing binaries are a major source of astrophysical false positives (*e.g.*, Sullivan et al. 2015, Figure 30). Our follow-up data showed that this and related scenarios were unlikely to the degree that we could validate the planet, *i.e.*, determine that its probability of being an astrophysical false positive was small. We considered this result worth reporting because of the planet's youth.

Section 2 describes the identification of the candidate, and our follow-up observations. Section 3 combines the available data to assess the system's false positive probability, and validates TOI 837b as a planet. Section 4 presents our knowledge of the cluster (Section 4.1), the star (Section 4.2) and

the planet (Section 4.3). We conclude by discussing avenues for confirmation and improved characterization in Section 5.

2. IDENTIFICATION AND FOLLOW-UP OBSERVATIONS

2.1. *TESS Photometry*

TOI 837 was observed by TESS from 26 March 2019 until 20 May 2019, during Sector 10 and Sector 11 of science operations (Ricker et al. 2015). The star was designated TIC 460205581 in the TESS Input Catalog (Stassun et al. 2018, 2019). Pixel data for an 11×11 array surrounding the star were co-added and saved at 2-minute cadence. The 2048×2048 image from the entire CCD was also co-added into 30-minute stacks, and saved as a "full frame image" (FFI).

The TESS Science Processing Operations Center (Jenkins et al. 2016) processed the image data and identified the transiting planet signature from two transits in Sector 10, again with three transits in Sector 11, and then for a final time when Sectors 1–13 were searched at the end of the first year of the mission. The transit signature was fitted with a limb-darkened transit model (Li et al. 2019) and passed all the diagnostic tests (Twicken et al. 2018), including the odd/even depth test, the weak secondary eclipse test, and the difference image centroiding test, which placed the transit source within ~ 2 arcsec of the location of TOI 837. No additional transit-like features were identified in any of the SPOC searches. The TESS Science Office alerted the community to this candidate transiting planet on 17 June 2019. Our subsequent blind search of the CDIPS FFI light curves also showed the transits, as did that of Nardiello et al. (2020). Given that the 2-minute data had better sampling cadence, we opted to use the Presearch Data Conditioning (PDC) light curve with the default aperture for our analysis (Smith et al. 2012; Stumpe et al. 2014; Smith et al. 2016).

The top panel of Figure 1 shows the TESS data. The dominant modulation induced by starspots coming into and out of view has a peak-to-peak amplitude of about 2.3%, and a period of about 3 days. The dips are suggestive of a grazing transiting planet, recurring roughly every 8 days with a depth of about 0.4%. A few flares are also visible. A phase-folded view of the TESS transits combined with ground-based follow-up photometry is shown in the bottom panel of Figure 1. The ground-based data and our fitting procedure are discussed in Sections 2.4 and 4.3 respectively. First though, some prerequisite context on the stellar neighborhood of TOI 837 is needed.

2.2. *Gaia Astrometry and Imaging*

Between 25 July 2014 and 23 May 2016, the ESA Gaia satellite measured about 300 billion centroid positions of 1.6 billion stars. The positions, proper motions, and parallaxes of the brightest 1.3 billion were calculated for the second data release (DR2) (Gaia Collaboration et al. 2016; Lindegren et al. 2018; Gaia Collaboration et al. 2018). TOI 837 was assigned the Gaia DR2 identifier 5251470948229949568, and had 276 "good" astrometric observations. Its brightness was
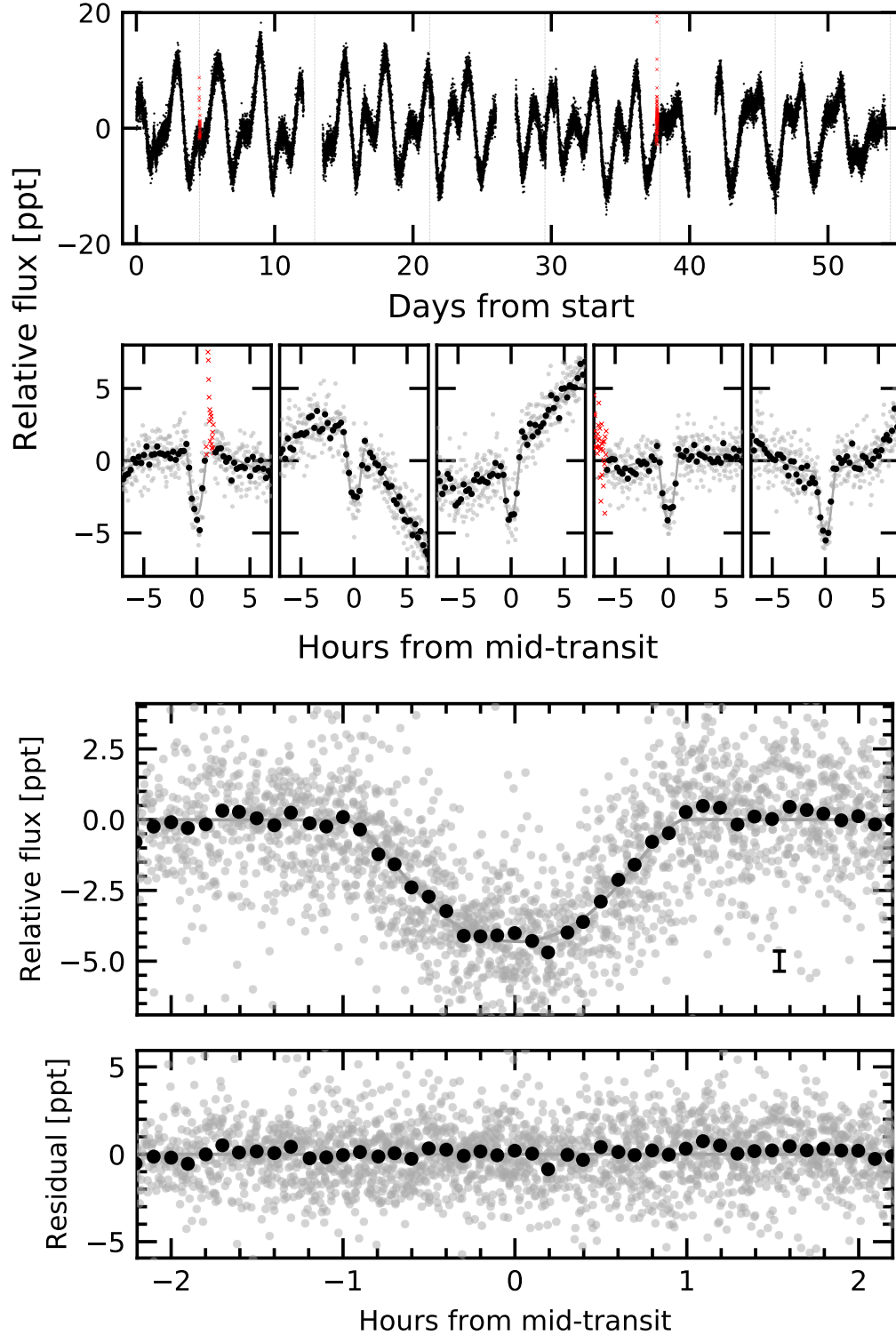
---

[1] ARCHIVE.STSCI.EDU/HLSP/CDIPS

Figure 1. Light curves of TOI 837. *Top*: TESS `PDCSAP` median-subtracted relative flux at 2-minute sampling in units of parts-per-thousand ($\times 10^{-3}$). Starspot-induced variability is the dominant signal; flares are shown with red crosses. Dashed lines indicate the five transits observed by TESS over Sectors 10 and 11. *Middle*: Individual TESS transits. Gray lines are the best-fit model to the TESS and ground-based data, which includes a local quadratic trend for each transit. Gray points are 2-minute `PDCSAP` flux measurements, black points are binned to 15-minute intervals. *Bottom*: Phase-folded TESS and ground-based transits. Section 2.4 presents the ground-based data. Gray points are flux measurements with the local spot-induced variation removed. A weighted binning at 6-minute intervals yields the black points. The black error-bar shows the median uncertainty for the black points. The gray line is the best-fit model for the entire dataset.
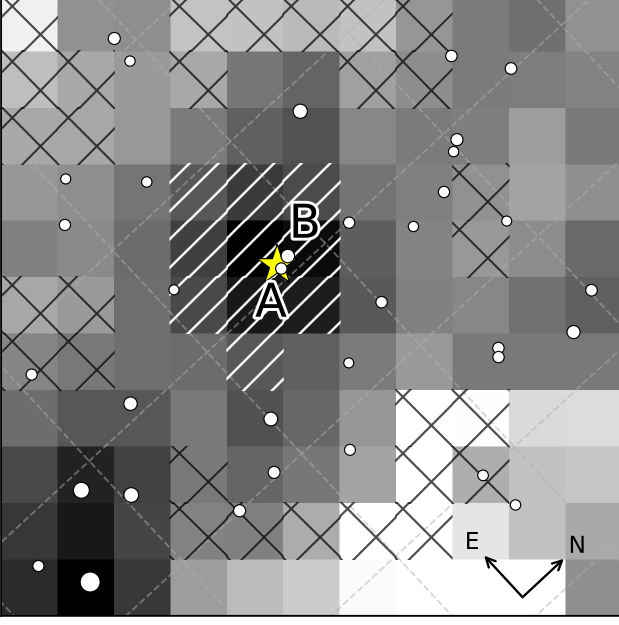
Figure 2. Scene of TOI 837. Mean TESS image of TOI 837 from Sector 10 on an 11×11 pixel cutout, with a logarithmic grayscale indicating the flux in each pixel. The yellow star is the position of TOI 837. White circles are resolved Gaia sources with $T < 16$, with brighter stars being larger. The black X and white / hatches show the apertures used to measure the background and target star flux, respectively. The compass shows cardinal directions in celestial coordinates. Dashed lines of constant declination are separated by $1'$, while those of right ascension are separated by $2'$. Two stars of interest are "Star A" and "Star B", which were excluded as being possible sources of the transits.

measured in the G, Rp, and Bp bands of the Radial Velocity Spectrometer (Cropper et al. 2018; Evans et al. 2018).

The Gaia imaging, reduced to its point-source catalog, provides the initial context for analyzing the TESS data. Stars brighter than $T = 16$, as queried from the Gaia DR2 source catalog, are shown with white circles in Figure 2, overlaid on the TESS image. Given its galactic latitude of $b = -6°$, it is not surprising that the field of TOI 837 is crowded. The resolved stars that were of immediate concern for our false positive analysis were as follows.

- TOI 837 $\equiv$ TIC 460205581 ($T = 9.9$). The target star.

- Star A $\equiv$ TIC 847769574 ($T = 14.6$), $2.3''$ West. The proper motions and parallax of this star imply it is co-moving with TOI 837 and that the two stars are separated by 6.6 ± 0.1 pc. Star A is therefore likely an IC 2602 member, but unlikely to be a bound binary companion.

- Star B $\equiv$ TIC 460205587 ($T = 13.1$), $5.4''$ North. The Gaia parallax implies this is a background giant star.
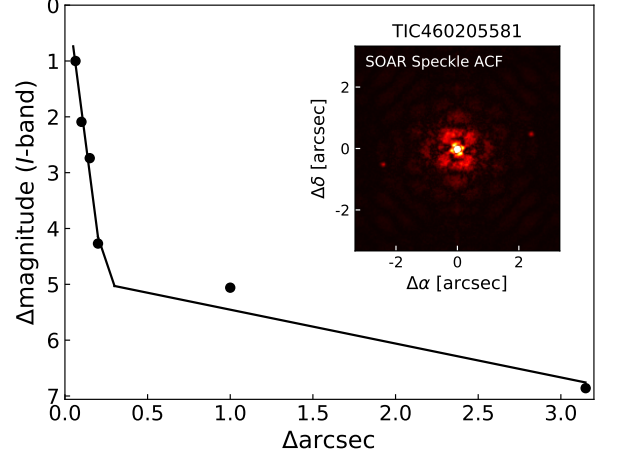

Figure 3. Speckle-imaging of TOI 837. Contrast limits from SOAR HRCam imaging were derived from point-source injection-recovery experiments. Star A ($\Delta T = 4.7$, $2.3''$ West) is detected, and is also a resolved Gaia source. It is co-moving with TOI 837, and its parallax and on-sky position imply that it is physically separated from TOI 837 by 6.6 ± 0.1 pc.

An additional source, TIC 847769581, is $4.9''$ from the target, but too faint ($T = 18.8$) to be the source of the observed transit signal.

The Gaia DR2 data for Star A seems poorly behaved. While Star A has $G = 15.1$, and $Bp = 14.9$, no Rp magnitude is reported. Correspondingly, no RUWE[2] value is available. We suspect that the photometric failure to produce an Rp magnitude as well as the poor astrometric fit of this star are due to blending with TOI 837.

At the $\approx 1'$ resolution of the TESS data, if either Star A or Star B were eclipsing binaries, they could be the sources of the transit signal. A detailed analysis of ground-based seeing-limited photometry was necessary to assess and rule out this possibility (Section 2.4 and Figure 4).

2.3. *High-Resolution Imaging*

To determine if any fainter point sources existed closer to TOI 837 inside of Gaia's point-source detection limits, we acquired high-resolution speckle images. We then searched the autocorrelation functions of these images for peaks indicative of nearby companions.

The observations of TOI 837 were initially acquired by Ziegler et al. (2020) as part of the Southern Astrophysical Research (SOAR) TESS Survey using the High Resolution Camera (HRCam; Tokovinin 2018). The HRCam I-band filter is described by Tokovinin (2018). The points in Figure 3 show the resulting measured 5-σ detectable contrasts. The lines are linear smoothing fits between the regimes of the diffraction limit, the "knee" at $\approx 0.2''$, and the slow decrease until $\approx 1.5''$, beyond which the speckle patterns be-
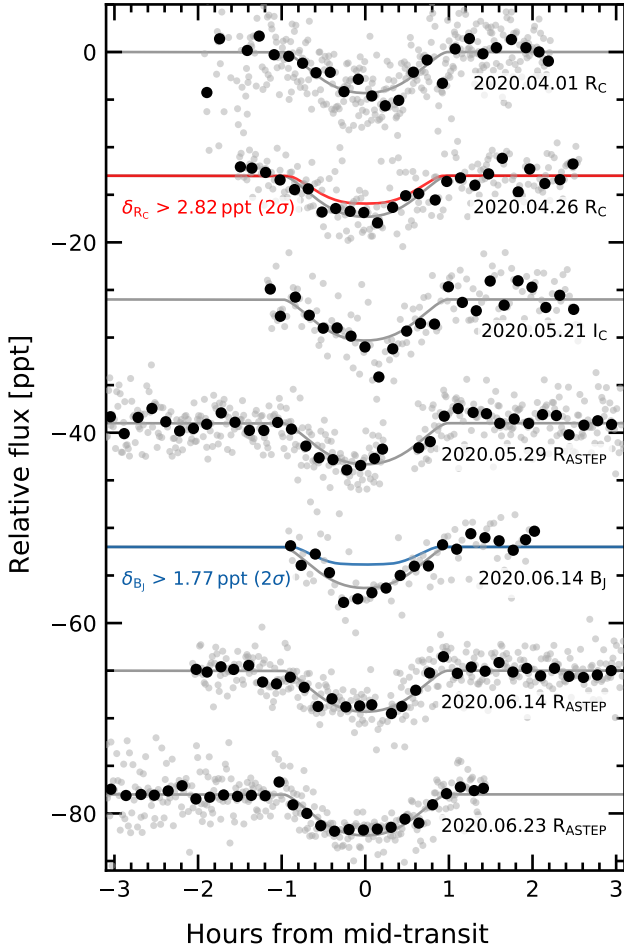

Figure 4. Ground-based follow-up photometry. The data were acquired using the 0.36 m telescope at El Sauce and the 0.40 m ASTEP400 telescope at Dome C. Black points represent the measurements after binning at 10-minute intervals. The gray line is the model that best fits the combined TESS and ground-based data. Red and blue lines show 2-σ lower limits on the transit depths in the Cousins-R and Johnson-B bandpasses used to rule out specific false positive scenarios (see Section 3.1.5).

come de-correlated. Star A (TIC 847769574) was detected at the expected location and brightness contrast, and no additional companions were found. Star B was not detected; with a separation of 5.4″ from TOI 837, it fell outside the field of view.

2.4. *Ground-based Time-Series Photometric Follow-up*

We obtained ground-based seeing-limited time series photometric observations of TOI 837 bracketed around the times of transit. These observations confirmed that the transits occurred on-target to within ≈ 2″, and that they were achromatic. Both features are essential for our ability to eliminate false-positive scenarios.

2.4.1. *El Sauce 0.36 m*

Acquisition and reduction—We observed four transits with the 0.36 m telescope at Observatorio El Sauce, located in the Río Hurtado Valley in Chile, and operated by co-author P. Evans. The observations were obtained in Cousins-R band on the nights of 1 April 2020 and 26 April 2020, Cousins-I band on the night of 21 May 2020, and Johnson-B band on the night of 14 June 2020. The final 14 June transit began shortly after twilight.

We scheduled our transit observations using the `TESS Transit Finder`, which is a customized version of the `Tapir` software package (Jensen 2013). The photometric data were calibrated and extracted using `AstroImageJ` (Collins et al. 2017). Comparison stars of similar brightness were used to produce the final light curves, each of which showed a roughly 4 ppt dip near the expected transit time. The data are reported in Table 1 and plotted in Figure 4.

Custom aperture analysis—Based solely on the TESS data, both Star A and Star B were possible sources of blended eclipsing binary signals. The typical FWHM for stars in the El Sauce observations was ≈ 2.3″, with a variance of ≈ 0.2″. Star B is resolved in the 0.36 m images; Star A is not.

To rule out blend scenarios with the ground-based photometry, we produced light curves centered on TOI 837 with circular apertures of radii ranging from 0.7″ to 5.1″. We did not detect any statistically significant variation in the depth of the transits with aperture size. Beyond the difference image centroiding test performed by the SPOC pipeline, two additional lines of evidence rule out Star B as the eclipsing source: first, the transits were detected in the smallest apertures. Second, we made light curves with 2.1″ apertures centered on Star B, and they did not show the transit.

To assess the possibility that Star A is an eclipsing body, we created light curves with a custom set of circular apertures with radii of 2.1″ and positions ranging from Star A (2.3″ West of TOI 837) to 2.3″ East of TOI 837. We did not detect any variation of the transit depth along this line of light curves. The apertures East of TOI 837 exclude over 90% of the flux from Star A. The eclipse on Star A would therefore need to have depth greater than unity to produce the observed eclipse depth. We therefore interpret the lack of asymmetry between the Western-most (centered on Star A) and Eastern-most (furthest from Star A) light curves as conclusive evidence that TOI 837 is the source of the transit signal to within ≈ 2.0″. To verify self-consistency, we checked that the maximum dilution from Star A (≈ 1%) is less than the uncertainty of the transit depth measurements (≈ 15%), and so the lack of variation of transit depth with aperture location is consistent with TOI 837 being the source of transits.

An additional line of evidence for Star A not being the transit host was also noted by the referee. The G-band magnitude and the parallax suggest that Star A is an M dwarf. As a probable cluster member, it would have $Bp - Rp \approx 2.8$ (see Section 4.1.2), which corresponds roughly to a mass in the range of 0.15–0.45 $M_\odot$, or densities roughly in the range of 2–3 g cm^{-3} based on the PARSEC isochrones (Bressan et al.

2012; Chen et al. 2014, 2015; Marigo et al. 2017). These densities are inconsistent with those inferred from the transit fits in Section 4.3.

2.4.2. *ASTEP400*

We observed three transits with the 0.40 m ASTEP telescope at the Concordia base on the Antarctic Plateau (Daban et al. 2010). Concordia base is operated by the French and Italian polar institutes, IPEV and PNRA. Its position on the Antarctic Plateau allows it to take advantage of the continuous night during Austral winter. The weather is of photometric quality for about two-thirds of each winter (Crouzet et al. 2018).

ASTEP is equipped with a FLI Proline science camera with a KAF-16801E, 4096×4096 front-illuminated CCD. The camera has an image scale of 0.93 arcsec pixel^{-1} resulting in a $1° \times 1°$ corrected field of view. The focal instrument dichroic plate splits the beam into a blue wavelength channel for guiding, and a non-filtered red science channel roughly matching a Cousins-R transmission curve (Abe et al. 2013; Mékarnia et al. 2016). The images were processed on-site using an automated aperture photometry pipeline based on the `daophot` package of the IDL astronomy user's library (Landsman 1995).

TOI 837 was observed with ASTEP on 12 May 2020, 29 May 2020, 14 June 2020, and 23 June 2020 (UT). Except for 12 May, our observations were conducted under stable weather conditions, with clear skies, temperatures of about $-70°C$, and wind speeds less than $5 \, \mathrm{m \, s^{-1}}$. Due to their poor quality, we exclude from the analysis all data collected on 12 May. We found that the optimal calibrated light curves of TOI 837 correspond to an 11 pixel (10 arcsec) and 14 pixel (12 arcsec) radius aperture for observations carried out on June and May, respectively. The data are reported in Table 1, and plotted in Figure 4.

Table 1. Ground-based TOI 837 photometry.

Time [BTJD$_{TDB}$]	Rel. Flux	Rel. Flux Err.	Instrument
1940.487018	0.999998	0.002430	El Sauce
1998.700107	0.998675	0.001621	ASTEP

NOTE— Table 1 is published in its entirety in a machine-readable format. Two example entries are shown for guidance regarding form and content. To convert from BTJD to BJD, add 2,457,000. See Eastman et al. (2010) for descriptions of the barycentric and leap second corrections.

2.5. *Spectroscopic Follow-up*

Reconnaissance spectroscopic follow-up is an essential step in vetting planet candidates. Medium to high-resolution spectra enable physical characterization of the star and therefore planet. Reducing multiple spectra to radial velocities can enable planet mass measurements, and can also lead to limits on the mass of nearby companions. Finally, if there are close or bright companions, reconnaissance spectra can also reveal the presence of a secondary set of stellar lines.
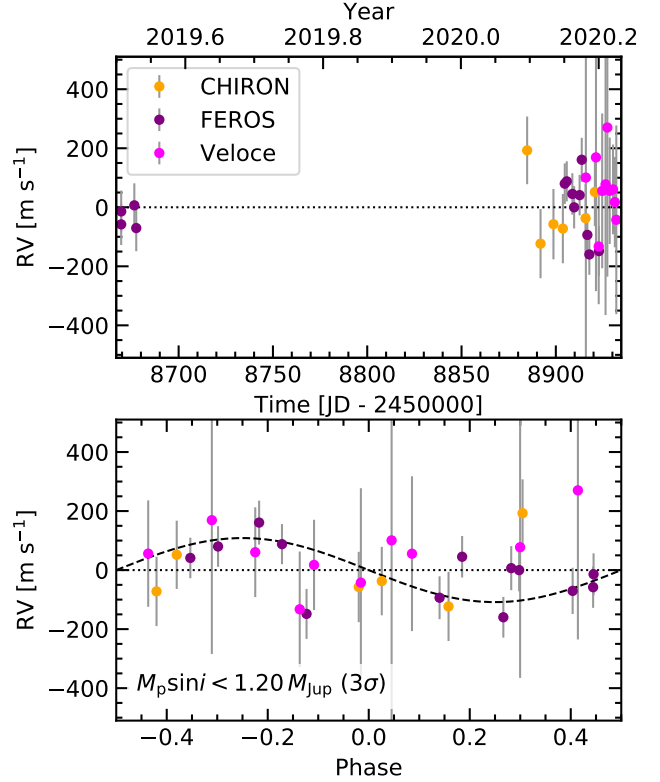

Figure 5. Velocimetry of TOI 837. *Top:* Radial velocity (RV) measurements, with best-fit instrument offsets and jitter terms included. The expected scatter from starspots based on $v \sin i$ and the photometric modulation amplitude is $\sim 300 \, \mathrm{m \, s^{-1}}$. *Bottom:* RV measurements phased to the orbital ephemeris of TOI 837b. The planet is not detected. The dashed black line shows a circular Keplerian orbit representing the 3-σ upper mass limit.

2.5.1. *SMARTS 1.5 m / CHIRON*

We acquired nine spectra using CHIRON at the SMARTS 1.5 m telescope at Cerro Tollo Inter-American Observatory, Chile (Tokovinin et al. 2013). Six met our signal-to-noise requirements for radial velocity measurements and stellar parameter extraction. We used CHIRON in its image slicer configuration, yielding a spectral resolution of $\approx 79,000$ across 415–880 nm.

We derived radial velocities and spectroscopic line profiles from the CHIRON observations using a least-squares deconvolution of the spectra against non-rotating synthetic spectral templates (Donati et al. 1997). The spectral templates were generated using ATLAS9 atmosphere models (Castelli & Kurucz 2004) with the `SPECTRUM` script (Gray & Corbally 1994). These line profiles were fitted with a broadening kernel that describes the rotational, radial-tangential macroturbulent, and instrumental broadening of the spectrum. The rotational and macroturbulent broadening are computed per Gray (2005), following the methods described in Zhou et al. (2018). We fitted the line profile from each observation independently, yielding the radial velocities listed in Table 2 and shown in Figure 5. We found a mean rotational broadening

velocity of $v \sin I_\star = 16.2 \pm 1.1 \, \mathrm{km \, s^{-1}}$, and a macroturbulent broadening of $v_{\mathrm{mac}} = 8.4 \pm 2.9 \, \mathrm{km \, s^{-1}}$.

To derive the stellar parameters, we matched the set of CHIRON spectra against a library of observed spectra, previously obtained using the Tillinghast Reflect Echelle Spectrograph (TRES, Fűrész et al. 2008) on the 1.5 m reflector at the Fred Lawrence Whipple Observatory (FLWO), Arizona, USA, and classified using the Stellar Parameter Classification pipeline (Buchhave et al. 2010). We found the best matching stellar parameters to be $T_{\mathrm{eff}} = 5899 \pm 55 \mathrm{K}$, $\log g = 4.496 \pm 0.011$ dex, and [Fe/H] $= -0.069 \pm 0.042$ dex. We ultimately adopted a different set of stellar parameters for our analysis (see Section 4.2.4).

The spectroscopic line profiles were thoroughly examined for any signs of secondary lines that might indicate the presence of another star, either associated or in chance alignment with TOI 837. No such set of lines was found. To set limits on the contributions of a close-by star to the observed spectrum, we injected a secondary signal into the mean least-squares deconvolution profile derived from the CHIRON observations. The injection spanned 10,000 different combinations of line broadening, velocity separation, and flux ratio F_2/F_1. The recovery results showed that for rotational broadenings of the secondary of 5, 15, and $25 \, \mathrm{km \, s^{-1}}$, we were able to exclude sources with flux fractions F_2/F_1 brighter than roughly 0.03, 0.08, and 0.20, provided that the secondary was separated from the primary by at least $\approx 15 \, \mathrm{km \, s^{-1}}$. At smaller velocity separations, the injected lines begin to blend with the target spectrum. We verified these results by injecting secondary lines directly into the spectrum and then deriving its LSD broadening profile as we would for a normal observation. The results were nearly identical, save for greater computational cost.

2.5.2. *FEROS*

TOI 837b was monitored with the FEROS echelle spectrograph (Kaufer et al. 1999), mounted on the MPG 2.2 m telescope at the ESO La Silla Observatory, in Chile. FEROS has a resolution of $\approx 48,000$ across a spectral range of 350–920 nm. It has a high efficiency of $\approx 20\%$. We obtained 13 spectra of TOI 837 between July 5 of 2019 and March 14 of 2020 in the context of the Warm gIaNts with tEss (WINE) collaboration, which focuses on the systematic characterization of TESS transiting giant planets with moderately long orbital periods (*e.g.*, Brahm et al. 2019; Jordán et al. 2020). We adopted exposure times of 500 and 600 seconds and the observations were performed with the simultaneous calibration mode for tracing the instrumental velocity variations with a comparison fiber illuminated with a ThAr lamp. FEROS data was processed with the `ceres` pipeline (Brahm et al. 2017), which delivers precision radial velocities and bisector span measurements through cross-correlation of the extracted spectra with a binary mask resembling the properties of a G2V star. The radial velocities are given in Table 2, and shown in Figure 5. To check for the presence of secondary lines, we performed a similar injection-recovery exercise as with the CHIRON data. We achieved slightly worse limits,

likely due to the lower spectral resolution of FEROS, and therefore adopted the CHIRON limits.

2.5.3. *Veloce*

We acquired 34 spectra over 10 visits of TOI 837 using the Veloce spectrograph, mounted on the 3.9 m Anglo-Australian Telescope at Siding Spring Observatory near Coonabarabran, Australia (Gilbert et al. 2018). The currently operational "Veloce-Rosso" channel provides coverage from 600–950 nm at a spectral resolution of $\approx 80,000$. Many of the exposures were taken in average or poor seeing conditions, when the SNR is lowest and the fiber-to-fiber cross-contamination on the IFU-style fiber feed is strongest. To reduce the spectra to velocities, we cross-correlated against a template of δ Pavonis, because with spectral type G8 IV it was the closest high-SNR TOI 837 analog available in the Veloce spectral database. The velocity RMS seen across each visit was hundreds of meters per second, likely due to uncorrected fiber-to-fiber cross-contamination. This cross-contamination severely affects the wavelength solutions for the 19 individual science fibres, ultimately leading to significantly increased RV scatter. For analysis purposes, we averaged the single-shot RVs across each visit, and set the velocity uncertainties to be the standard deviation of the per-visit exposures. The velocities are given in Table 2, and shown in Figure 5.

Table 2. TOI 837 radial velocities.

Time [$\mathrm{BJD_{TDB}}$]	RV [$\mathrm{m \, s^{-1}}$]	σ_{RV} [$\mathrm{m \, s^{-1}}$]	Instrument
8669.533150	-57.8	27.5	FEROS
8669.540450	-13.9	29.4	FEROS
8676.506930	6.7	37.8	FEROS
8677.519150	-70.3	44.6	FEROS
8884.787630	240.0	28.0	CHIRON
8891.891180	-76.0	37.0	CHIRON
8898.735330	-10.0	43.0	CHIRON
8903.725760	-25.0	38.0	CHIRON
8904.739930	80.1	24.5	FEROS
8905.793630	88.0	21.7	FEROS
8908.762520	45.3	28.3	FEROS
8909.702140	0.0	31.8	FEROS
8912.606750	41.3	24.1	FEROS
8913.740580	161.1	37.3	FEROS
8915.762170	10.0	33.0	CHIRON
8916.714540	-93.5	33.6	FEROS
8917.765720	-159.7	24.8	FEROS
8920.706100	99.0	32.0	CHIRON
8922.845800	-148.3	54.9	FEROS
8915.924027	37.5	725.9	Veloce
8921.284950	105.9	453.2	Veloce
8922.733572	-195.9	195.6	Veloce
8924.583708	-7.6	262.3	Veloce
8926.365810	14.3	442.6	Veloce
8927.318146	207.0	505.2	Veloce
8928.559780	-7.3	180.2	Veloce

Table 2 *continued*

Table 2 *(continued)*

Time [BJD$_{\rm TDB}$]	RV [m s^{-1}]	$\sigma_{\rm RV}$ [m s^{-1}]	Instrument
8930.324059	-2.6	152.0	Veloce
8931.293091	-45.7	152.9	Veloce
8932.065206	-105.6	319.8	Veloce

3. ASSESSMENT OF FALSE POSITIVE SCENARIOS

Validating a transiting planet means statistically arguing that the data are much more likely to be explained by a planet than by an astrophysical false positive. The concept of validation has been developed and calibrated by *e.g.*, Torres et al. (2011); Morton (2012); Díaz et al. (2014); Santerne et al. (2015); Morton et al. (2016) and Giacalone & Dressing (2020). "Validation" is different from "confirmation", which means that there is overwhelming evidence that the transits *must* be explained by a planet, through elimination of all false positive scenarios and determination that the planet's mass is in the substellar regime.

Assuming an eclipse has been localized to the target star, potential false positive scenarios include eclipses of an unresolved background binary (BEB), eclipses of a hierarchical system bound to the primary star (HEB), and the possibility that the eclipses are caused by a stellar companion, rather than a planetary one (EB).

Figure 6 provides a visual summary of the possible astrophysical false positive scenarios, as well as our ability to rule them out based on our combined photometry, velocimetry, and imaging. In this Section we describe each constraint in turn, and then present a calculation using VESPA (Morton 2012) to demonstrate that the probability of TOI 837 being an astrophysical false positive is small enough to validate it as a planet.

3.1. *Constraints on False Positive Scenarios*

3.1.1. *Transit Depth*

In HEB and BEB scenarios, the flux from TOI 837 and the true eclipsing binary host blend together, and reduce the "true" TESS-band eclipse depth $\delta_{\rm true}$ to the observed depth $\delta_{\rm obs}$:

$$\delta_{\rm obs} = \delta_{\rm true} \frac{F_{\rm comp}}{F_{\rm total}}, \quad (1)$$

where the total system flux and the flux from only the companion ("comp") binary are labeled as such. The requirement that the eclipse is produced by fusion-powered stars and that $\delta_{\rm true} < 0.5$ translates to a bound on the faintest possible blended companion system:

$$\Delta m < -\frac{5}{2} \log_{10} \left(\frac{0.5}{\delta_{\rm obs}} \right). \quad (2)$$

For TOI 837 ($T = 9.93$), this implies that any stellar companion invoked to explain the transit depth must be brighter than $T = 15.07$. In Figure 6, we set the spatial limit to $2''$ based on the precision at which we have localized the transits using seeing-limited ground-based photometry.

If the transit were box-shaped, this argument could be extended to even more restrictive depths (*e.g.*, Seager & Mallén-Ornelas 2003; Vanderburg et al. 2019; Rizzuto et al. 2020). Since the transits of TOI 837 could be grazing, the second and third contact points do not necessarily occur, and the shape of the transit is not particularly restrictive.

3.1.2. *Speckle Imaging*

The contrast limits obtained through the SOAR *I*-band speckle imaging (Section 2.3) are shown in Figure 6. While "Star A" was detected in the SOAR images, our ground-based photometry rules it out as a possible source of the eclipse signal (Section 2.4). To convert the remaining contrast constraints to limits on the masses of bound companions, we used the Baraffe et al. (2003) models for sub-stellar mass objects and the MIST models for stellar mass objects (Paxton et al. 2011, 2013, 2015; Dotter 2016; Choi et al. 2016). We assumed that the system age was 35 Myr, so that companions would be at a plausible state of contraction.

To convert from theoretical effective temperatures and bolometric luminosities to expected magnitudes in instrumental bandpasses, we made the simplifying assumption that all sources had blackbody spectra. Using the theoretical stellar parameters and the measured transmission functions (Tokovinin 2018), we then calculated the apparent magnitudes of stellar companions of different masses, and interpolated to produce the scale shown on the upper-right in Figure 6.

3.1.3. *Not SB2*

We derived limits on blended spectroscopic companions using the stacked CHIRON spectra (see Section 2.5.1). For a slowly rotating stellar companion well-separated in velocity, the spectra would have revealed companions with flux fractions $F_2/F_1 \gtrsim 3\%$. For a companion with rotational broadening of $15\,{\rm km\,s}^{-1}$, roughly equivalent to that of TOI 837, we were able to exclude companions with flux fractions exceeding $\approx 8\%$. For plotting purposes, in Figure 6 we have assumed the latter flux-fraction limit of 8% (Δmag ≈ 2.7). The outer limit in projected separation for associated companions is the distance at which the Keplerian orbital velocity is well below the rotational broadening. This condition translates to a projected separation of 10–20 AU, depending on the companion mass. For chance alignments, the same restrictions on velocity separation apply, but out to a projected separation equal to the CHIRON slit width of $\approx 1''$.

3.1.4. *RVs*

The radial velocities from FEROS, CHIRON, and Veloce can be used to detect massive bound companions orbiting TOI 837. We searched for planetary and stellar-mass companions in two different regimes: first, at the orbital period of the transiting object, and second, at longer orbital periods to constrain the presence of a massive bound companion.

For the first fit we set a prior on the period and time of conjunction using the known ephemeris from the transit. We
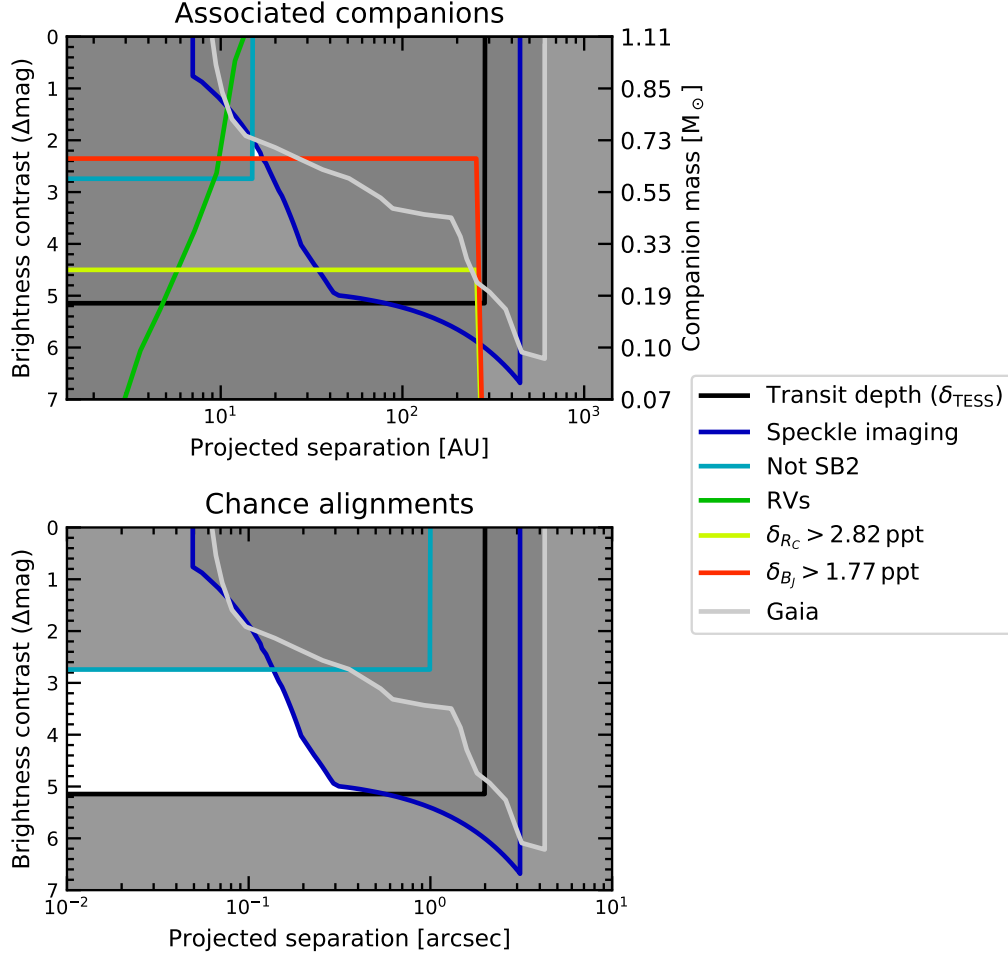
Associated companions

Chance alignments

Figure 6. Astrophysical false positive scenarios. *Top*: for bound companions (EB and HEB scenarios), *Bottom*: for unassociated companions along the same line of sight (BEB scenarios). Each constraint is described in Section 3.1. Gray regions are ruled out by at least one constraint.

then fitted for the semi-amplitude, instrument offsets, and jitter parameters using `radvel` (Fulton et al. 2018), and assuming circular orbits. This yielded a non-detection of the planet's orbit. The corresponding 3-σ (99.7$^{\rm th}$ percentile) upper limit on $M_{\rm p} \sin i$ is $1.20 M_{\rm Jup}$. The data and corresponding model are shown in Figure 5.

The above exercise ruled out the possibility that the observed eclipses are caused by a stellar-mass object orbiting TOI 837. The lack of a linear radial velocity trend, particularly in the FEROS data, further constrains the presence of a hierarchical binary system. Fitting a line to the FEROS velocities yielded a 3-σ limit on linear radial velocity trends of $|\dot{\gamma}| < 0.82 \, {\rm m \, s^{-1} \, day^{-1}}$, over the 253 day FEROS baseline. The agreement between the mean Gaia DR2 velocity ($17.44 \pm 0.64 \, {\rm km \, s^{-1}}$) and that from FEROS ($18.0 \pm 0.1 \, {\rm km \, s^{-1}}$) in theory places an additional limit on linear trends, since the two observation epochs are separated by roughly five years.

To place limits on the properties of a possible bound hierarchical companion, we performed the following injection-recovery exercise. We simulated 10^6 two-body systems with random orbital phases and inclinations, and drew their

semi-amplitudes and periods from logarithmic distributions: $K \, [{\rm m \, s^{-1}}] \sim \log \mathcal{U}(1, 10^7)$, and $P \, [{\rm days}] \sim \log \mathcal{U}(1, 10^{15})$. Again assuming circular orbits, we then analytically evaluated what the radial velocities would have been at the observed FEROS times if the system had the assumed parameters. We then calculated what the linear slope would have been for each simulated system. If the absolute value of the slope exceeded our 3-σ limit of $|\dot{\gamma}| < 0.82 \, {\rm m \, s^{-1} \, day^{-1}}$, we assumed that we would have detected such a system. Figure 6 shows the resulting limits; weakened sensitivity at harmonics of the baseline occur at lower masses and smaller projected separations than shown on the plot. The interpolation from mass to brightness contrast was performed using the same isochrone models and assumptions as in Section 3.1.2.

3.1.5. *Multicolor Photometry*

Multicolor photometry and HEB scenarios—The most plausible HEB scenarios for TOI 837 involve pairs of eclipsing M dwarfs (Figure 6). Eclipses of such stars are much redder than eclipses of the G-dwarf TOI 837. Limits on whether the transit depth decreases in bluer bandpasses can therefore rule out certain HEB scenarios.

We fitted for the observed depths in different bandpasses using a machinery similar to that described below in Section 4.3. We fitted each ground-based transit individually for the planet-to-star size ratio, the impact parameter, and a local quadratic trend (the ephemeris was assumed from an initial fit of only the TESS data). The corresponding 2-σ lower limits on the transit depths in Cousins-R and Johnson-B band light curves were 2.82 and 1.77 ppt, respectively, and are shown in Figure 4. Particularly in our Johnson-B light curve, the transit depth is correlated with the mean and linear slope of the light curve: a smaller depth is allowed if the data are fitted with a larger linear slope and a larger mean. Our quoted limits marginalize over these correlations, and the depth measurement itself is nearly Gaussian.

To determine what classes of HEB are eliminated by these limits, we performed the following calculation. We assumed that each system was composed of the primary (TOI 837), plus a tertiary companion eclipsing a secondary companion every 8.3 days. For secondary masses ranging from 0.07 to 1.10 $M_\odot$, and mass ratios (M_3/M_2) from 0.1 to 1, we then calculated the observed maximal eclipse depth caused by Star 3 eclipsing Star 2 in each observed bandpass. As before, we interpolated between mass, effective temperature, and radius assuming the MIST isochrones for a 35 Myr old system, and also assumed that each source had a blackbody spectrum. We used the transmission functions from the SVO filter profile service[3]. For a typical HEB system (*e.g.*, $M_2 = M_3 = 0.2 M_\odot$), the bluest optical bandpasses produced eclipses roughly 10 times shallower than in TESS-band, because the M-dwarf blackbody function turns over at much redder wavelengths than the G-dwarf blackbody (Wien's law).

For a fixed secondary mass, we then asked whether any tertiary companions existed for which the maximal expected eclipse depth could have been larger than the observed depth. We could not rule out hierarchical eclipsing binary systems in cases for which the answer was yes. Conversely, we ruled out systems for which at fixed secondary mass no tertiary mass could enable eclipses of the necessary depth (in R_C-band, or in B_J-band). The R_C-band limit corresponded to a secondary mass limit of $M_2 > 0.27 M_\odot$, and the B_J-band corresponded to a stronger limit of $M_2 > 0.70 M_\odot$.

Multicolor photometry and BEB scenarios —While the above constraints rule out HEBs, certain configurations of BEB systems (*e.g.*, a background G0V+K3V binary) can produce blue eclipses while remaining undetected along the line of sight. Such scenarios are constrained by the lack of an observed secondary eclipse, and therefore require either eccentric orbits to avoid secondary eclipses, or else a background twin binary system at double the orbital period. The only way to definitively rule out such scenarios is to prove that the loss of light is from the target star, for instance by detecting the Rossiter-McLaughlin effect during a transit, and confirming

that the spectroscopic transit is consistent with the photometric transit.

3.1.6. *Gaia*

The "Gaia" curve in Figure 6 combines both point-source detections from imaging and sources showing an astrometric noise excess relative to the single-source astrometric model. The curve was interpolated from Figure 4 of Rizzuto et al. (2018). TOI 837 has a RUWE statistic of 1.022, indicative that there are no obviously present astrometric companions. The UWE statistic (square-root of the reduced astrometric χ^2) is 1.38, which is consistent with stars of similar brightness and color (Lindegren et al. 2018, Appendix A).

3.1.7. *Patient Imaging*

Archival SERC-J and AAO-SES plates are available for the TOI 837 field[4]. These plates were acquired in 1982 and 1992, respectively. For high proper motion stars archival imagery can be used to detect slowly moving background stars that might be an astrophysical false-positive source (*e.g.*, Bakos et al. 2006; Huang et al. 2018b; Vanderburg et al. 2019). However TOI 837 has only moved $\approx 0.7''$ between 1982 and present, in comparison to the $\approx 2.0''$ FWHM of the target on the plates. We therefore cannot resolve it from background sources not already resolved through more modern imaging.

3.2. *False positive probability*

The constraints on false-positive scenarios summarized in Figure 6 rule out the possibilities that *i)* the eclipses are caused by a star orbiting TOI 837, *ii)* the eclipses are caused by hierarchical blends[5], and *iii)* the eclipses are caused by neighboring stars outside $\approx 2''$. The only scenario not formally ruled out is a background eclipsing binary. A simple, and fallacious, argument against background blends follows from counting statistics. The local density of $T < 15.1$ stars around TOI 837, found by counting from TIC8, is 3.7×10^{-4} arcsec^{-2}. Therefore within the relevant $\approx 0.3''$ radius not excluded by the SOAR HRCam contrast curve, for a randomly selected star we would expect 1.0×10^{-4} potential $T < 15.1$ contaminants, which appears small.

The reason the above statement is an insufficient argument against BEBs is that TOI 837 is not a randomly selected star—it was selected because it shows eclipses. Given a foreground star that shows eclipses, the probability of a background star being present is much greater than for an arbitrary foreground star. A probabilistic framework is required to calculate the chance that a background eclipsing binary causes the eclipses. We adopt the Bayesian framework implemented in VESPA (Morton 2012, 2015b).

---

[3] http://svo2.cab.inta-csic.es/theory/fps/

[4] https://archive.stsci.edu/cgi-bin/dss_form

[5] There is a small gap in the upper panel of Figure 6, corresponding to a $\approx 0.7 M_\odot$ companion HEB at a projected separation of ≈ 15 AU. This region of parameter space is small, and we ignore it in the remaining analysis.

VESPA calculates the false positive probability for a transit signal as

$$FPP = 1 - P_{pl}, \qquad (3)$$

where in our case the probability that the signal comes from a planet, P_{pl}, is given by

$$P_{pl} = \frac{\mathcal{L}_{pl}\pi_{pl}}{\mathcal{L}_{pl}\pi_{pl} + \mathcal{L}_{BEB}\pi_{BEB}}, \qquad (4)$$

where $\mathcal{L}_i$ is the model likelihood for the planet and BEB scenarios, and π_i is the model prior. The terms labeled as "BEB" usually include other false positive scenarios (HEBs and EBs), but our followup data have excluded these possibilities. The priors are evaluated using a combination of galactic population synthesis (Girardi et al. 2005), binary star statistics (Raghavan et al. 2010), and specific planet occurrence rates (Morton 2012, Section 3.4). The likelihoods are evaluated by forward-modeling a representative population of eclipsing bodies for each model class, in which each population member has a particular trapezoidal eclipse depth, total duration, and ingress duration. The likelihood is then calculated by multiplying the probability distribution function of the simulated population's shape parameters with the posterior probability of the actual observed eclipse shape.

We ran VESPA[6], and directly incorporated our constraints of the SOAR I-band contrast curve and a non-detection of secondary eclipses with a depth set at roughly twice the limits from the SPOC vetting report (0.1%). This limit applies across all phases. We verified that changing the secondary eclipse depth limit did not significantly affect the results. We set the maximum aperture radius at $2''$, based on our ground-based photometry. Incorporating the constraints from Figure 6, our nominal false positive probability analysis excluded EB and HEB scenarios. This yielded an FPP of 0.21% for TOI 837b, sufficient for formal validation as a planet (Morton 2012). We did not incorporate our constraint that TOI 837 is not double-lined, which rules out an additional portion of BEB parameter space. Had we not acquired multicolor ground-based photometry, and been unable to exclude HEB scenarios, the FPP would have risen to 8%. Since the transits are achromatic (Figure 4), particularly in Johnson-B band, we can rule out HEB scenarios.

One potential caveat in our approach is that VESPA uses a galactic population synthesis to model the sight-line. Since TOI 837 is in the foreground of IC 2602 (see Section 4.2), for roughly 25 pc behind the sightline to the star, the number of background stars is higher than VESPA would predict due to the presence of the cluster. To quantify the importance of this effect, we assessed the sky-plane density of potential contaminants by counting stars brighter than $T = 15.07$ within 0.5 degrees of TOI 837 (Stassun et al. 2019). We then compared this density against sightlines rotated in galactic longitude towards and away from the galactic center. Within $\pm 10°$ in galactic longitude, the sky-plane density of stars fluctuated

---

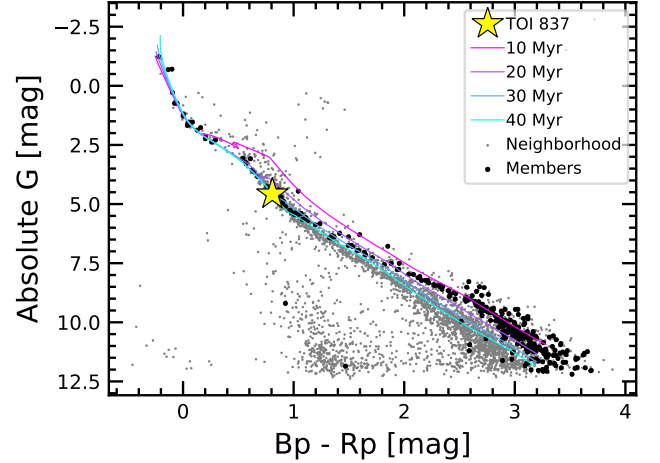[6] We used VESPA-0.6 and isochrones-1.2.2.

Figure 7. Hertzsprung-Russell diagram of TOI 837 and members of IC 2602. Members (black circles) were identified by Cantat-Gaudin et al. (2018). Gray circles are non-member stars with right ascension, declination, and parallax similar to IC 2602. They are selected by drawing from a $\{\alpha, \delta, \pi\}$ cube centered on the cluster with boundaries set at $5\times$ the standard deviation in the cluster parameters. G denotes Gaia broadband magnitudes, Bp Gaia blue, and Rp Gaia red. MIST isochrones (colored lines) fit the upper main sequence well, but diverge from the data for $M_\star \lesssim 0.7 M_\odot$. This is a known issue with the M dwarf models (see Section 4.1.2).

at the level of $\approx 15\%$, with a local maximum a few degrees away from TOI 837, towards the center of IC 2602. The overall density also slowly increased towards the galactic center. We therefore do not expect this consideration to significantly alter our FPP calculation.

4. SYSTEM MODELING

4.1. *The Cluster*

4.1.1. *Physical Characteristics*

The IC 2602 cluster is about 150 pc from the Earth, and is near the galactic plane with $(l, b) \approx (289.6°, -5.0°)$ (Cantat-Gaudin et al. 2018). It is also sometimes called the θ Carinae cluster, after its brightest member, or also the "Southern Pleiades". While IC 2602 is close to the Lower Centaurus Crux subgroup of the Scorpio-Centaurus OB2 association in both position and proper motion space, its older age and clear kinematic separation indicate that it is a distinct stellar population (de Zeeuw et al. 1999; Damiani et al. 2019).

Reliable ages reported for IC 2602 range from 30 to 46 Myr. We have collected ages reported over the years in Table 3. The Li depletion boundary technique yields slightly older absolute ages than isochrone fitting (Dobbie et al. 2010; Randich et al. 2018). Rather than redetermine the age of the cluster and add another line to the table, we simply adopt an absolute age range for TOI 837 of 30–46 Myr.

Reported mean metallicity values [Fe/H] for the cluster range between slightly super-solar (0.04 ± 0.01, Baratella et al. 2020) and slightly sub-solar (-0.02 ± 0.02, Netopil et al.

Figure 8. Positions and kinematics of TOI 837 (star), IC 2602 members (black circles), and stars in the neighborhood (gray circles).
Members were identified by Cantat-Gaudin et al. (2018). Neighbors are as in Figure 7. α denotes right ascension, δ declination, π parallax, μ_δ and μ_α proper motion in each equatorial direction, and RV radial velocity reported by Gaia DR2. The RVs are for unblended spectra of bright stars ($G \lesssim 12$). The proper motion projection (μ_δ vs. $\mu_\alpha \cos \delta$) highlights incompleteness in the membership selection function.

2016). The extinction $E(B-V)$ is rather low, with reported values ranging from 0.03 to 0.07 (*e.g.*, Randich et al. 2018).

Kinematically, IC 2602 seems to be supervirial, in the sense that the observed stellar velocity dispersion is larger than the value expected if it were in virial equilibrium by about a factor of two (Bravi et al. 2018). Damiani et al. (2019) also reported evidence for the ongoing evaporation of IC 2602, in the form of a diffuse $\approx 10°$ halo of young stars around the central density cusps. A gyrochronological study of these stars could confirm that these stars are truly coeval with the cluster.

4.1.2. *HR Diagram*

Figure 7 shows a Hertzsprung-Russell diagram of TOI 837, the IC 2602 cluster, and the neighborhood of spatially nearby stars. Stars labeled as cluster members are those reported by Cantat-Gaudin et al. (2018) based on Gaia DR2 positions, proper motions, and parallaxes. We included candidate members with formal membership probability exceeding 10%. Most members appear to be young and coeval. TOI 837 lies on the single-star sequence. Any hypothetical companions to TOI 837 must therefore be $\lesssim 50\%$ of its brightness; brighter companions would have made the total system $\gtrsim 0.44$ mag-

nitudes brighter than the single-star sequence, which can be ruled out based on the photometric uncertainties and the intrinsic scatter in the HR diagram.

Figure 7 suggests that the membership census of IC 2602 is incomplete. We defined the reference neighborhood as the group of at most 10^4 randomly selected non-member stars within 5 standard deviations of the mean IC 2602 right ascension, declination, and parallax. In other words, the neighborhood members are chosen based on the observed spread in the cluster's parameters. We queried Gaia DR2 for these stars using `astroquery` (Ginsburg et al. 2018). Many low-mass stars appear above the main sequence, even though they were not identified as 5-dimensional kinematic members through the unsupervised Cantat-Gaudin et al. (2018) membership assignment process.

Figure 7 also compares the data to the MIST isochrones (Choi et al. 2016). We used the web interface[7] to interpolate isochrones at 10, 20, 30, and 40 million years. We assumed solar metallicity, and a fixed extinction value of $A_V = 0.217$ (Randich et al. 2018). The 30 and 40 Myr models align well

---

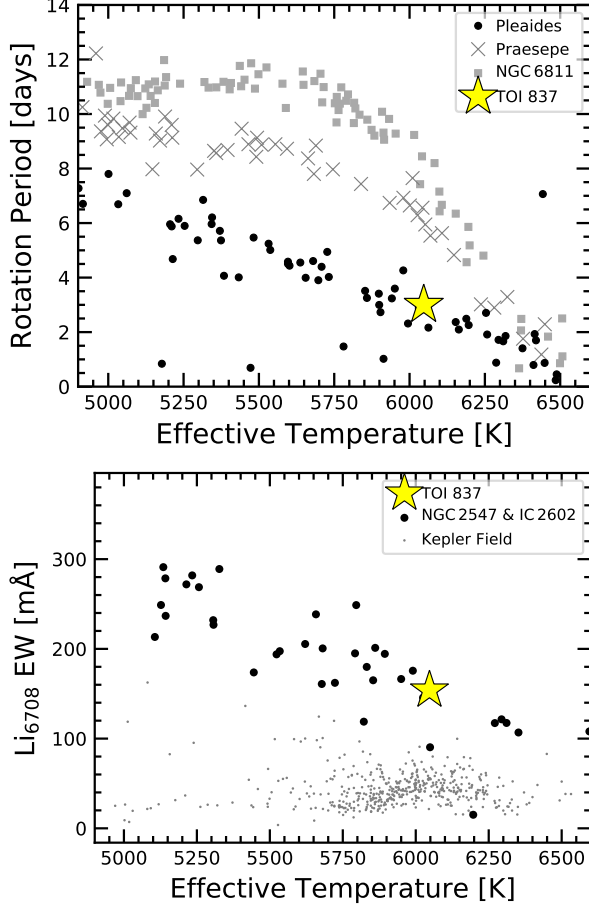[7] http://waps.cfa.harvard.edu/MIST/interp_isos.html, 2020-07-08

Figure 9. Youth diagnostics. *Top:* Rotation periods for TOI 837 and selected open clusters. The Pleiades (120 Myr), Praesepe (670 Myr), and NGC 6811 (1000 Myr) are shown. Their rotation periods were measured by Rebull et al. (2016); Douglas et al. (2017, 2019), and Curtis et al. (2019a), respectively. *Bottom:* Lithium 6708Å equivalent widths for TOI 837, field stars, and young open clusters. The field star sample is drawn from Kepler planet hosts, and was measured by Berger et al. (2018) using Keck-HIRES. The young open cluster members were surveyed by Randich et al. (2018) using the UVES and GIRAFFE spectrographs at the ESO VLT. Randich et al. (2018) found lithium depletion boundary ages for these clusters of $37.7^{+5.7}_{-4.8}$ Myr (NGC 2547) and $43.7^{+4.3}_{-3.9}$ Myr (IC 2602).

with the data for stars with masses ranging from roughly 0.7–$7 M_\odot$. The pre-main-sequence (PMS) K and M dwarf models are bluer than observed in the Gaia photometry. This discrepancy was noted and discussed at length by Choi et al. (2016). One suggested explanation was that strong magnetic fields in low-mass pre-main-sequence stars inhibit convection and produce a high filling factor of starspots (*e.g.*, Stauffer et al. 2003; Feiden & Chaboyer 2013). This explanation however fails to explain poor isochrone fits in both old open clusters (*e.g.*, M 67) and the field, particularly in blue bandpasses. An alternative explanation is that the molecular line

Table 3. Previously reported ages for the open cluster IC 2602.

Method	Age [Myr]	Reference
MSTO isochrone	36.3	Mermilliod (1981)
PMS+MSTO isochrone	30 ± 5	Stauffer et al. (1997)
Isochrone (a)	67.6	Kharchenko et al. (2005)
Isochrone (b)	221	Kharchenko et al. (2013)
Isochrone	67.6	van Leeuwen (2009)
LDB (c)	46^{+6}_{-5}	Dobbie et al. (2010)
MSTO isochrone (d)	$41 - 46$	David & Hillenbrand (2015)
MSTO isochrone (e)	$37 - 43$	David & Hillenbrand (2015)
Li selection + isochrone	$43.7^{+4.3}_{-3.9}$	Bravi et al. (2018)
Isochrone (f)	30^{+9}_{-7}	Randich et al. (2018)
LDB	$43.7^{+4.3}_{-3.9}$	Randich et al. (2018)
Isochrone	$35.5^{+0.8}_{-1.6}$	Bossini et al. (2019)
Isochrone	$35.5^{+14.6}_{-10.4}$	Kounkel & Covey (2019)

NOTE— MSTO ≡ main sequence turn-off. PMS ≡ pre-main-sequence. LDB ≡ lithium depletion boundary. (a) Based on location in HR diagram of just two stars. (b) Notes major age change since Kharchenko et al. (2005). (c) Dobbie et al. (2010) performed a dedicated study of the LDB in IC 2602. Comparing to early isochronal ages, they write their age is "consistent with the general trend delineated by the Pleiades, α-Per, IC 2391, and NGC 2457, whereby the LDB age is 120-160 per cent of the estimates derived using more traditional techniques" such as isochrone fitting. (d) Using Ekström et al. (2012) evolutionary models. (e) Using PARSEC evolutionary models (Bressan et al. 2012). (f) Averaged across PROSECCO, PARSEC, MIST models in (J, H, K_s) and (J, H, K_s, V) planes.

lists for M dwarf atmospheres are incomplete in these wavelength ranges (Rajpurohit et al. 2013; Mann et al. 2013).

4.2. *The Star*

4.2.1. *Membership of TOI 837 in IC 2602*

TOI 837 has been reported as a member of IC 2602 by many independent investigators (*e.g.*, Kharchenko et al. 2013; Oh et al. 2017; Cantat-Gaudin et al. 2018; Damiani et al. 2019; Kounkel & Covey 2019). The simplest way to verify the membership is through inspection of the Gaia DR2 position and kinematics. Figure 8 shows the six-dimensional positions and kinematics of TOI 837, IC 2602 members, and nearby stars. The "neighborhood" is defined as in Figure 7. The axes limits for the right ascension, declination, and parallax dimensions are set by being within 5 standard deviations of the mean IC 2602 right ascension, declination, and parallax. The axes limits for the proper motion and radial velocity dimensions are set at the 25th and 75th percentiles, in order to give a sense of the population's distribution, while excluding outliers. The radial velocities suffer the greatest incompleteness due to the current $G \approx 12$ magnitude limit of the Gaia DR2 data processing.

Figure 8 provides strong evidence that TOI 837 is a member of IC 2602. The only dimension that could lead to some worry is the parallax, as TOI 837 is one of the closest IC 2602 members reported by Cantat-Gaudin et al. (2018). Fortunately, there are independent means of verifying the star's youth.

4.2.2. *Rotation*

As stars get older, their rotation rates incrementally slow due to magnetic braking Weber & Davis (1967); Skumanich

(1972). One way to verify the youth of TOI 837 is by comparing its rotation period to other stars with known ages.

We measured the rotation period from the TESS PDCSAP light curve using the Lomb-Scargle periodogram implemented in astropy (Lomb 1976; Scargle 1982; VanderPlas & Ivezić 2015). We fitted the light curve without masking out the transits or flares, as these represent a small fraction of the overall time series. To derive the uncertainty on the best period, we fitted a Gaussian to the dominant peak, after first ensuring that we had oversampled the initial frequency grid. This gave a rotation period of $P_{\rm rot} = 2.987 \pm 0.056$ d when allowing for a single Fourier term in the periodogram model, and $P_{\rm rot} = 3.004 \pm 0.053$ d when allowing for two Fourier terms. As the latter model provides a better fit to the data, we adopt it as the rotation period.

As we will discuss in Section 4.2.4, we measured the star's radius by combining the spectroscopic effective temperature with a broadband photometry SED fit. We would expect, combining our $R_\star$ and $P_{\rm rot}$ measurements, that the equatorial velocity v of the star would be $17.67 \pm 0.32\,{\rm km\,s^{-1}}$. Our spectroscopically measured $v \sin i$ from CHIRON, $16.2 \pm 1.1\,{\rm km\,s^{-1}}$ agrees reasonably well with this expectation.

The star is clearly a rapid rotator. Figure 9 compares its rotation period with rotation periods that have been measured in a number of well-studied open clusters. TOI 837 seems to be gyrochronologically coeval with the Pleiades sequence. This is not to say that TOI 837 is "Pleiades-aged", because the observed scatter in the rotation-period diagram for the first 10–100 Myr is quite high (see Figure 9 of Rebull et al. 2020). Instead, we interpret the rotation period as evidence to support the claim that TOI 837 is younger than ~ 500 Myr.

4.2.3. *Lithium*

Lithium depletion for early G-dwarfs like TOI 837 requires hundreds of megayears (Soderblom et al. 2014). This is because their convective envelopes are shallow, and so transport of photospheric lithium to the hot core takes place over diffusive timescales, rather than convective timescales. Nonetheless, comparison of early G-dwarfs in the field to *e.g.*, 600 Myr old Hyads has shown that the depletion does indeed happen over many gigayears (Berger et al. 2018).

The spectra of TOI 837 all show the 6708 Å lithium doublet in absorption. Opting to use our FEROS spectra because of their high S/N, we measured the line's equivalent width (EW) to be 154 ± 9 mÅ. Figure 9 compares this EW to stars in the field, and other young open cluster members. The field star measurements were collected by Berger et al. (2018); we show their reported lithium detections with S/N > 3. The young open cluster members were selected for the presence of lithium, as described by Randich et al. (2018). The measured TOI 837 Li EW is much larger than observed for field stars, and is consistent with lithium absorption seen in stars with similar colors in sub-100 Myr moving groups.

4.2.4. *Stellar Parameters*

Select properties of TOI 837 from the literature and our analysis are presented in Table 4. We calculated the stellar parameters using two different approaches.

In "Method 1", we measured spectroscopic parameters from each of the CHIRON spectra (Section 2.5.1). We then calculated the stellar radius and reddening following Stassun et al. (2017). We first derived the bolometric flux by combining available broadband magnitudes from Gaia, Tycho-2, APASS, 2MASS, and WISE. We then fitted the SED with the Kurucz (2013) stellar atmopshere models, and summed to find $F_{\rm bol}$. When fitting the atmosphere model, we varied the extinction ($A_{\rm V}$) and the overall normalization. This procedure yielded $A_{\rm V} = 0.20 \pm 0.03$, which agrees with the average from the IC 2602 isochrone fits of Randich et al. (2018). Combining the spectroscopic effective temperature, bolometric flux, and Gaia distance, we determined the stellar radius using the Stefan-Boltzmann law. Combining this radius with the spectroscopic $\log g$ also yields a stellar mass. The stellar mass however seemed to be high relative to the observed CHIRON effective temperature ($1.21 M_\odot$ to 5946 K, with relative uncertainties of a few percent on each). We therefore explored a second method, and ultimately adopted it because its systematic uncertainties were easier to quantify.

In "Method 2", we used the observed location of TOI 837 in the HR diagram and interpolated against the 40 Myr MIST isochrone. This method leverages the relative location of TOI 837 within the IC 2602 isochrone to derive precise, theoretically self-consistent constraints on all of the stellar parameters. Although this approach would fail for a low-mass star, TOI 837 is above the stellar masses where the Gaia photometry and isochrone models begin to diverge. The statistical uncertainties yielded by this approach are of order 1% for the stellar mass and radius. To quantify the systematic uncertainties, we compared the parameters derived from the MIST isochrones with those from the PARSEC[8] isochrones (Bressan et al. 2012; Chen et al. 2014, 2015; Marigo et al. 2017). The PARSEC isochrones gave a stellar mass 5% lower, effective temperature 3% lower, logarithmic surface gravity 1% lower, and radius 8% lower than the MIST isochrones. For the sake of self-consistency, in Table 4 and the ensuing analysis we adopted the stellar parameter values from MIST. We took the uncertainties to be the quadrature sum of the statistical and systematic components.

4.3. *The Planet*

We also considered two different approaches for fitting the available time-series photometry of TOI 837b. In the first approach, we fitted the ground and space-based transits simultaneously. In the second, we fitted the TESS data alone.

To clean the TESS PDCSAP light curve, we first eliminated points that had quality flags corresponding to any of bits $\{3, 4, 6, 8, 11, 12\}$. This excluded cadences affected by coarse spacecraft pointing, reaction wheel desaturation events, manual flags, cosmic ray hits, and straylight from the Earth or
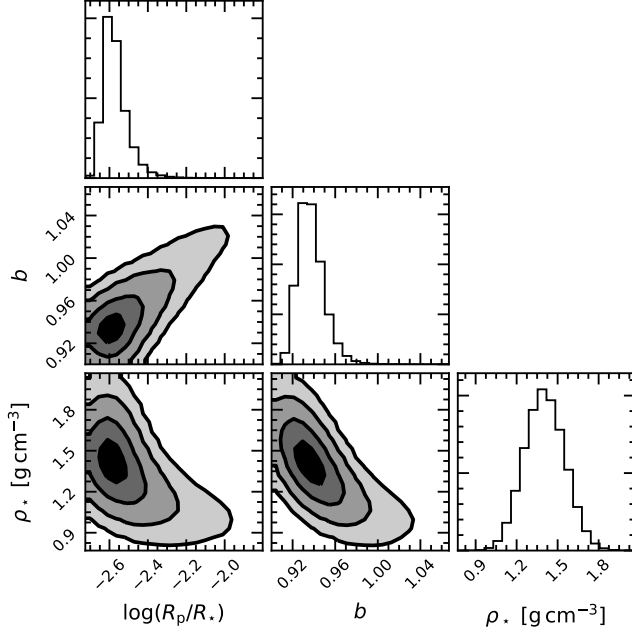
---

[8] http://stev.oapd.inaf.it/cmd

Figure 10. Posterior probabilities of impact parameter, planet-to-star size ratio, and stellar density. Contours are shown at 1, 2, 3, and 4-σ confidence. The planet-to-star size ratio corresponds to a planet size between $0.62\,R_{\mathrm{Jup}}$ and $0.95\,R_{\mathrm{Jup}}$ (3$^{\mathrm{rd}}$–97$^{\mathrm{th}}$ percentile). This plot was made using `corner` (Foreman-Mackey 2016).

Moon being present. Inspecting the data, we also manually excluded the two flares shown in Figure 1. We then trimmed the TESS data to windows of $\pm 7\,\mathrm{hr}$ centered on each transit.

Our model for time-series photometry data was an Agol et al. (2020) transit with physical and orbital parameters shared across all transit windows, plus a local quadratic trend allowed within each window. Select parameters and priors are listed in Table 5, for the joint model of the TESS and ground-based data. In brief, we fitted for the shared stellar parameters $\{\log g, R_\star, u_0, u_1\}$, and the shared planetary parameters $\{t_0, P, b, \log(R_{\mathrm{p}}/R_\star)\}$. There were also three free trend parameters for each transit window to account for the local rotational variability. In the TESS-only model this yielded 23 free parameters, of which 8 were physically relevant and 15 were nuisance parameters. In the combined TESS and ground-based model, there were an additional 7 transits, and therefore an additional 21 nuisance parameters for a total of 44 free parameters.

We fitted the models using `PyMC3` (Salvatier et al. 2016; Theano Development Team 2016). For the exoplanet transit, we used the `exoplanet` code (Foreman-Mackey et al. 2020). After initializing each model with the parameters of the maximum *a posteriori* model, we assumed a Gaussian likelihood, and sampled using `PyMC3`'s gradient-based No-U-Turn Sampler (Hoffman & Gelman 2014). We used $\hat{R}$ as our convergence diagnostic (Gelman & Rubin 1992).

We opted for this approach rather than a joint fit of the photometry and radial velocities because the RVs on their own did not show evidence for a planetary signal. Our assump-

tion of a constant radius across all bandpasses was tested by independently fitting each ground-based transit while letting the planetary radius float (Section 3.1.5). The transit depths did not significantly change between different bandpasses. Our assumption in the false-positive probability calculation (Section 3.2) of no odd-even variations was tested by independently fitting all odd and all even transits separately. The resulting best-fit depths were consistent within 1-σ.

The posteriors from fitting the TESS and ground-based data are given in Table 5. The condition for a grazing transit is whether the impact parameter b is above $1 - R_{\mathrm{p}}/R_\star$. The relevant posterior probabilities are shown in Figure 10. The transit is either grazing, or nearly grazing. The planet radius and impact parameter based on the TESS and ground-based data are as follows.

$$R_{\mathrm{p}} = 0.768^{+0.091}_{-0.072}\,R_{\mathrm{Jup}}, \tag{5}$$

$$b = 0.936^{+0.013}_{-0.010}, \tag{6}$$

where we quote the median, 86$^{\mathrm{th}}$, and 14$^{\mathrm{th}}$ percentiles of the marginalized one-dimensional posteriors.

The second model, which used just the TESS data and the cluster-isochrone stellar parameter priors, formally yielded only a one-sided limit on the planet radius. The reason is that the b–$R_{\mathrm{p}}/R_\star$ degeneracy was not broken: the combination of uncertain stellar parameters and the grazing geometry allowed very large planet-to-star radius ratios for very large impact parameters. Based on our mass upper limit of $1.20\,M_{\mathrm{Jup}}$, we might argue in favor of discarding the large-radius solution, since no sub-Jovian mass objects larger than $\sim 3R_{\mathrm{Jup}}$ are known to exist. Had we imposed this additional prior, then the TESS-only model would have yielded

$$R_{\mathrm{p}} = 0.836^{+0.208}_{-0.121}\,R_{\mathrm{Jup}} \tag{7}$$

$$b = 0.957^{+0.027}_{-0.017}. \tag{8}$$

Although these parameters are in 1-σ agreement with our adopted joint model of the TESS and ground-based data, we preferred the first model both because it included all available data, and because it succeeded in breaking the b–$R_{\mathrm{p}}/R_\star$ degeneracy without requiring the adoption of informed priors.

5. DISCUSSION

TOI 837 joins a number of other young planetary systems reported from TESS, including DS Tuc Ab, HIP 67522b, TOI 1726, and AU Mic b (Newton et al. 2019; Zhou et al. 2020; Montet et al. 2020; Rizzuto et al. 2020; Mann et al. 2020; Plavchan et al. 2020; Palle et al. 2020; Addison et al. 2020; Martioli et al. 2020; Hirano et al. 2020). In the space of planet sizes and ages, the top panel of Figure 11 shows that TOI 837 is among the youngest transiting planets known.

In the space of planet sizes and orbital periods, the bottom panel of Figure 11 highlights a peculiar feature of the known sub-100 Myr transiting planets: they do not overlap with the known populations of either hot Jupiters or sub-Neptune sized planets. The young planets instead have sizes
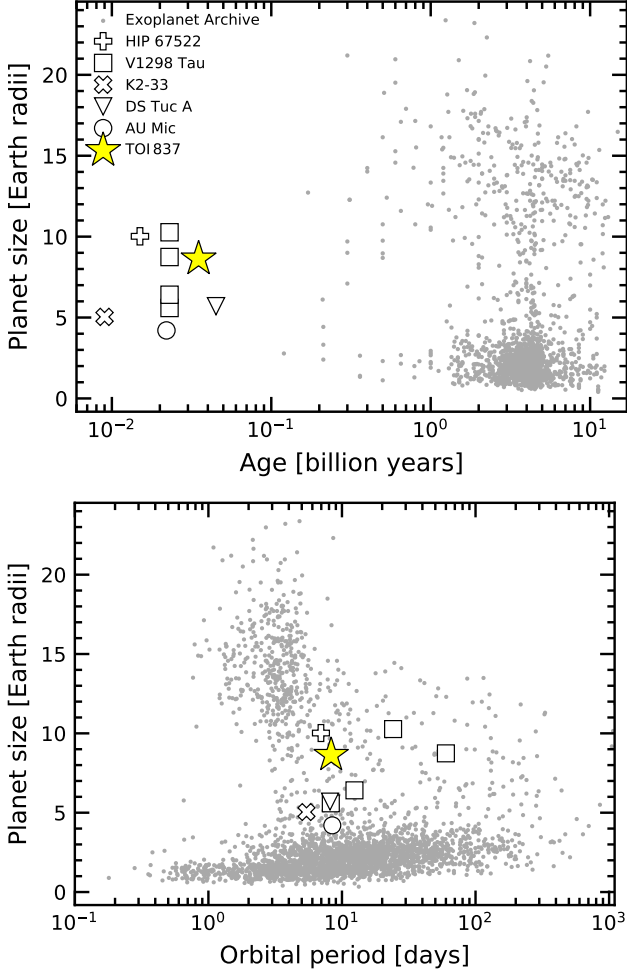
Figure 11. TOI 837 compared to known transiting planets. *Top*: Planet radii versus ages. Systems younger than 100 Myr are emphasized. Ages and radii are from the NASA Exoplanet Archive on 27 Aug 2020. Precise ages are known for only a small fraction of the gray points. *Bottom*: Planet radii versus orbital periods. The youngest known transiting planets do not obviously overlap with the populations of known hot Jupiters or sub-Neptunes.

ranging from $4.2\,R_\oplus$ (AU Mic b) to slightly smaller than Jupiter. The lack of sub-Neptune sized planets could be a selection effect, because larger planets are easier to detect around highly variable stars. Another (speculative) explanation is that the known sub-100 Myr planets are currently enveloped by primordial H/He atmospheres, and that they will become sub-Neptune sized planets after undergoing atmospheric escape (*e.g.*, Fortney et al. 2007; Owen & Wu 2013; Gupta & Schlichting 2019, 2020).

While we have statistically validated that TOI 837 is a planet, the possibility that it could be a background eclipsing binary has not been excluded with sufficient confidence to call the planet "confirmed". The distinction is methodological. Our calculations have shown that at a population level we expect negligibly few BEBs within $\approx 0.3''$ of TOI 837 to pro-

duce eclipses of the appropriate shape across all bandpasses, with no observed secondary eclipse or odd-even variations. This statement is tautologically "validation", but it is weaker than having data on hand that conclusively rules in favor of the planetary interpretation.

The easiest way to confirm the planetary nature of TOI 837 will be a Rossiter-McLaughlin (RM) measurement. Detection of an RM signal consistent with the photometric transit would rule out BEB and HEB scenarios, as it would imply that the eclipsing object is bound to the target star. Combined with our non-detection of the planet's mass from radial velocity monitoring, this would confirm that TOI 837b is a planet.

The maximum amplitude of the Rossiter-McLaughlin anomaly is (Gaudi & Winn 2007)

$$\Delta V_{\mathrm{RM}} \approx f_{\mathrm{LD}} \cdot \delta \cdot v \sin i \cdot \sqrt{1-b^2} \approx 14\,\mathrm{m\,s^{-1}}, \qquad (9)$$

for

$$f_{\mathrm{LD}} = 1 - u_1(1-\mu) - u_2(1-\mu)^2, \qquad (10)$$

where $\mu \approx (1-b^2)^{1/2}$, u_i are the limb-darkening parameters, and for calculation purposes we assumed $b = 0.95$ and used stellar and transit parameters from Tables 4 and 5. Although challenging, for a 1.9 hr transit of a $V = 10.6$ star, a detection could be achieved with modern spectrographs. The next viable total transit windows from Chile occur in January and February of 2021; there are also a few visible per season from other southern locations. The most precise available ephemeris, found from our joint fit of the TESS and ground-based photometry, is as follows.

$$t_0\ [\mathrm{BJD_{TDB}}] = 2458574.272527 \pm 0.000593$$
$$P\ [\mathrm{d}] = 8.3248762 \pm 0.0000157$$
$$T_{14}\ [\mathrm{hr}] = 1.96 \pm 0.04. \qquad (11)$$

The Rossiter-McLaughlin approach is more likely to yield short-term success than a direct mass measurement because of the RV noise expected to be induced by stellar rotation. The photometric amplitude induced by starspots on TOI 837 is $\approx 2\%$. The spot-induced RV variation expected over the course of the ≈ 3 d rotation period can be estimated by multiplying the photometric amplitude and spectroscopic equatorial velocity. This gives $\sigma_{\mathrm{RV,rot}} \approx 300\,\mathrm{m\,s^{-1}}$, and is consistent with the scatter we observe in our radial velocities from FEROS. Detecting a planet's Keplerian motion in this regime is challenging, and requires a significant amount of data and care in signal extraction (Barragán et al. 2019). The Rossiter-McLaughlin measurement avoids the majority of this issue because the transit occurs over a much shorter duration than a single stellar rotation period.

If the RM measurements prove that the validated planet is real, measuring its mass may be worth the effort, because it would improve understanding of the planet's composition and future atmospheric evolution. If an RV campaign were timed to coincide with TESS Sectors 36 and 37 (3 March

2021 through 28 April 2021), it would significantly ease extraction of the Keplerian signal. The reason is that the RVs, activity indicators, and photometry could be modeled simultaneously (*e.g.*, Aigrain et al. 2012; Rajpaul et al. 2015). Combining photometric and radial velocity data from non-overlapping epochs would also constrain the models, but perhaps not quite as convincingly.

While we hope that RV observations will be pursued, data acquired during the TESS mission extension may also help in understanding the system (Bouma et al. 2017; Huang et al. 2018a). In particular, additional photometry will likely enable more detailed exploration of whether the orbit of TOI 837 is eccentric, and also whether the system could host additional transiting planets.

Table 4. Literature and Measured Properties for TOI 837

Other identifiers			
	TIC 460205581		
	GAIADR2 5251470948229949568		

Parameter	Description	Value	Source
$\alpha_{J2015.5}$	Right Ascension (hh:mm:ss)	10:28:08.95	1
$\delta_{J2015.5}$	Declination (dd:mm:ss)	-64:30:18.76	1
$l_{J2015.5}$	Galactic Longitude (deg)	288.2644	1
$b_{J2015.5}$	Galactic Latitude (deg)	-5.7950	1
B	Johnson B mag.	11.119 ± 0.107	2
V	Johnson V mag.	10.635 ± 0.020	2
G	Gaia G mag.	10.356 ± 0.020	1
Bp	Gaia Bp mag.	10.695 ± 0.020	1
Rp	Gaia Rp mag.	9.887 ± 0.020	1
T	TESS mag.	9.9322 ± 0.006	2
J	2MASS J mag.	9.392 ± 0.030	3
H	2MASS H mag.	9.108 ± 0.038	3
K_S	2MASS K_S mag.	8.933 ± 0.026	3
W1	WISE1 mag.	8.901 ± 0.023	4
W2	WISE2 mag.	8.875 ± 0.021	4
W3	WISE3 mag.	8.875 ± 0.020	4
W4	WISE4 mag.	$8.936 \pm N/A$	4
π	Gaia DR2 parallax (mas)	6.989 ± 0.022	1
d	Distance (pc)	143.1 ± 0.5	1
μ_α	Gaia DR2 proper motion	-18.017 ± 0.039	1
	in RA (mas yr^{-1})		
μ_δ	Gaia DR2 proper motion	11.307 ± 0.037	1
	in DEC (mas yr^{-1})		
RV	Systemic radial	17.44 ± 0.64[†]	1
	velocity (km s^{-1})		
$v \sin i_\star$	Rotational velocity (km s^{-1})	16.2 ± 1.1	5
v_{mac}	Macroturbulence velocity (km s^{-1})	8.4 ± 2.9	5
[Fe/H]	Metallicity	-0.069 ± 0.042	5
T_{eff}	Effective Temperature (K)	6047 ± 162	6
$\log g_\star$	Surface Gravity (cgs)	4.467 ± 0.049	6
Li EW	6708Å Equiv. Width (mÅ)	154 ± 9	7
P_{rot}	Rotation period (d)	3.004 ± 0.053	8
Age	Adopted stellar age (Myr)	30–46	9
Spec. Type	Spectral Type	G0/F9 V	5
$R_\star$	Stellar radius ($R_\odot$)	1.022 ± 0.083	6
$M_\star$	Stellar mass ($R_\odot$)	1.118 ± 0.059	6
A_V	Interstellar reddening (mag)	0.20 ± 0.03	10

NOTE— † Systemic RV uncertainty is the standard deviation of single-transit radial velocities, as quoted in Gaia DR2. Provenances are: [1]Gaia Collaboration et al. (2018), [2]Stassun et al. (2019), [3]Skrutskie et al. (2006), [4]Wright et al. (2010), [5]CHIRON spectra, [6]Method 2 (cluster isochrone, Section 4.2.4), [7]FEROS spectra, [8]TESS light curve, [9]IC 2602 ages from isochrone & lithium depletion analyses (Section 4.1.1), [10]Method 1 (photometric SED fit, Section 4.2.4).

Table 5. Priors and posteriors for the model fitted to the TESS and ground-based data.

Param.	Unit	Prior	Median	Mean	Std. Dev.	3%	97%
Sampled: physical							
P	d	$\mathcal{N}(8.3249; 0.1000)$	8.3248762	8.3248762	0.0000157	8.3248466	8.3249057
$t_0^{(1)}$	d	$\mathcal{N}(1574.273800; 0.1000)$	1574.272527	1574.2725263	0.0005931	1574.2713991	1574.273626
$\log R_{\rm p}/R_\star$	–	$\mathcal{U}(-4.605; 0.000)$	-2.58156	-2.56901	0.06659	-2.67426	-2.44791
b	–	$\mathcal{U}(0; 1+R_{\rm p}/R_\star)$	0.9358	0.9374	0.0127	0.9164	0.9615
u_1	–	$\mathcal{U}(0.175; 0.475)^{(2)}$	0.344	0.338	0.085	0.199	0.475
u_2	–	$\mathcal{U}(0.085; 0.385)^{(2)}$	0.251	0.245	0.085	0.108	0.385
$R_\star$	$R_\odot$	$\mathcal{T}(1.022; 0.083)$	1.042	1.042	0.076	0.902	1.189
$\log g$	cgs	$\mathcal{N}(4.467; 0.049)$	4.451	4.451	0.042	4.372	4.528
Sampled: nuisance							
$a_{00;\rm TESS}$	–	$\mathcal{N}(1.00; 0.01)$	0.9986	0.9986	0.0001	0.9984	0.9987
$a_{01;\rm TESS}$	$\rm d^{-1}$	$\mathcal{U}(-0.05; 0.05)$	-0.0004	-0.0004	0.0003	-0.0010	0.0003
$a_{02;\rm TESS}$	$\rm d^{-2}$	$\mathcal{U}(-0.05; 0.05)$	-0.0183	-0.0183	0.0023	-0.0226	-0.0141
$a_{10;\rm TESS}$	–	$\mathcal{N}(1.00; 0.01)$	1.0090	1.0090	0.0001	1.0088	1.0092
$a_{11;\rm TESS}$	$\rm d^{-1}$	$\mathcal{U}(-0.05; 0.05)$	-0.0138	-0.0138	0.0003	-0.0144	-0.0132
$a_{12;\rm TESS}$	$\rm d^{-2}$	$\mathcal{U}(-0.05; 0.05)$	-0.0550	-0.0550	0.0022	-0.0591	-0.0508
$a_{20;\rm TESS}$	–	$\mathcal{N}(1.00; 0.01)$	0.9992	0.9992	0.0001	0.9990	0.9993
$a_{21;\rm TESS}$	$\rm d^{-1}$	$\mathcal{U}(-0.05; 0.05)$	0.0156	0.0156	0.0004	0.0150	0.0163
$a_{22;\rm TESS}$	$\rm d^{-2}$	$\mathcal{U}(-0.05; 0.05)$	0.0232	0.0232	0.0024	0.0187	0.0276
$a_{30;\rm TESS}$	–	$\mathcal{N}(1.00; 0.01)$	1.0013	1.0013	0.0001	1.0011	1.0015
$a_{31;\rm TESS}$	$\rm d^{-1}$	$\mathcal{U}(-0.05; 0.05)$	0.0021	0.0021	0.0004	0.0014	0.0028
$a_{32;\rm TESS}$	$\rm d^{-2}$	$\mathcal{U}(-0.05; 0.05)$	-0.0097	-0.0097	0.0029	-0.0150	-0.0043
$a_{40;\rm TESS}$	–	$\mathcal{N}(1.00; 0.01)$	0.9906	0.9906	0.0001	0.9905	0.9908
$a_{41;\rm TESS}$	$\rm d^{-1}$	$\mathcal{U}(-0.05; 0.05)$	0.0015	0.0015	0.0003	0.0009	0.0022
$a_{42;\rm TESS}$	$\rm d^{-2}$	$\mathcal{U}(-0.05; 0.05)$	0.0313	0.0313	0.0023	0.0269	0.0356
$a_{00;\rm Sauce}$	–	$\mathcal{N}(1.00; 0.01)$	0.9996	0.9996	0.0001	0.9993	0.9998
$a_{01;\rm Sauce}$	$\rm d^{-1}$	$\mathcal{U}(-0.05; 0.05)$	-0.0041	-0.0041	0.0023	-0.0085	0.0002
$a_{02;\rm Sauce}$	$\rm d^{-2}$	$\mathcal{U}(-0.05; 0.05)$	0.0311	0.0256	0.0205	-0.0135	0.0500
$a_{10;\rm Sauce}$	–	$\mathcal{N}(1.00; 0.01)$	0.9998	0.9998	0.0001	0.9996	1.0000
$a_{11;\rm Sauce}$	$\rm d^{-1}$	$\mathcal{U}(-0.05; 0.05)$	-0.0004	-0.0004	0.0021	-0.0044	0.0035
$a_{12;\rm Sauce}$	$\rm d^{-2}$	$\mathcal{U}(-0.05; 0.05)$	0.0360	0.0314	0.0165	0.0005	0.05000
$a_{20;\rm Sauce}$	–	$\mathcal{N}(1.00; 0.01)$	0.9999	0.9999	0.0001	0.9996	1.0001
$a_{21;\rm Sauce}$	$\rm d^{-1}$	$\mathcal{U}(-0.05; 0.05)$	-0.0009	-0.0009	0.0030	-0.0066	0.0046
$a_{22;\rm Sauce}$	$\rm d^{-2}$	$\mathcal{U}(-0.05; 0.05)$	0.0067	0.0047	0.0278	-0.0410	0.0500
$a_{30;\rm Sauce}$	–	$\mathcal{N}(1.00; 0.01)$	0.9996	0.9996	0.0003	0.9991	1.0001
$a_{31;\rm Sauce}$	$\rm d^{-1}$	$\mathcal{U}(-0.05; 0.05)$	0.0047	0.0047	0.0069	-0.0084	0.0176
$a_{32;\rm Sauce}$	$\rm d^{-2}$	$\mathcal{U}(-0.05; 0.05)$	0.0077	0.0052	0.0286	-0.0419	0.0500
$a_{00;\rm ASTEP}$	–	$\mathcal{N}(1.00; 0.01)$	0.9996	0.9996	0.0001	0.9994	0.9998
$a_{01;\rm ASTEP}$	$\rm d^{-1}$	$\mathcal{U}(-0.05; 0.05)$	0.0022	0.0022	0.0007	0.0010	0.0035
$a_{02;\rm ASTEP}$	$\rm d^{-2}$	$\mathcal{U}(-0.05; 0.05)$	0.0073	0.0074	0.0076	-0.0067	0.0219
$a_{10;\rm ASTEP}$	–	$\mathcal{N}(1.00; 0.01)$	1.0000	1.0000	0.0001	0.9998	1.0002
$a_{11;\rm ASTEP}$	$\rm d^{-1}$	$\mathcal{U}(-0.05; 0.05)$	0.0042	0.0042	0.0010	0.0024	0.0061
$a_{12;\rm ASTEP}$	$\rm d^{-2}$	$\mathcal{U}(-0.05; 0.05)$	0.0164	0.0162	0.0145	-0.0105	0.0439
$a_{20;\rm ASTEP}$	–	$\mathcal{N}(1.00; 0.01)$	0.9993	0.9993	0.0001	0.9991	0.9995
$a_{21;\rm ASTEP}$	$\rm d^{-1}$	$\mathcal{U}(-0.05; 0.05)$	-0.0074	-0.0074	0.0016	-0.0103	-0.0044
$a_{22;\rm ASTEP}$	$\rm d^{-2}$	$\mathcal{U}(-0.05; 0.05)$	0.0204	0.0173	0.0216	-0.0209	0.0500
Derived							
$R_{\rm p}/R_\star$	–	–	0.08	0.08	0.01	0.07	0.09
$\rho_\star$	$\rm g\ cm^{-3}$	–	1.40	1.40	0.15	1.13	1.68
$R_{\rm p}$	$R_{\rm Jup}$	–	0.77	0.78	0.09	0.62	0.95
$a/R_\star$	–	–	17.26	17.24	0.60	16.12	18.36
$\cos i$	–	–	0.054	0.054	0.003	0.050	0.059
T_{14}	hr	–	1.957	1.955	0.039	1.887	2.032
T_{13}	hr	–	0.30	0.30	0.13	0.004	NaN$^{(3)}$

NOTE— (1) The most precise ephemeris based on the combination of TESS and ground-based data is also shown in Equation 11. (2) Assuming an informative quadratic limb-darkening prior with values about those given for the appropriate $T_{\rm eff}$ and $\log g$ in TESS-band from Claret (2017). The precision achieved in the ground-based data did not appear to necessitate using bandpass-dependent limb-darkening coefficients. (3) The second and third contact points do not exist for a grazing transit. *Notation*: $a_{ij;\rm Instr}$ denotes the $i^{\rm th}$ transit of a particular instrument, and the $j^{\rm th}$ polynomial detrending order. $\mathcal{U}$ denotes a uniform distribution, $\mathcal{N}$ a normal distribution, and $\mathcal{T}$ a truncated normal bounded between zero and an upper limit much larger than the mean.

REFERENCES

Abe, L., Gonçalves, I., Agabi, A., et al. 2013, A&A, 553, A49

Addison, B. C., Horner, J., Wittenmyer, R. A., et al. 2020, arXiv:2006.13675 [astro-ph]

Agol, E., Luger, R., & Foreman-Mackey, D. 2020, AJ, 159, 123

Aigrain, S., Hodgkin, S., Irwin, J., et al. 2007, MNRAS, 375, 29

Aigrain, S., Pont, F., & Zucker, S. 2012, MNRAS, 419, 3147

Angus, R., Aigrain, S., Foreman-Mackey, D., & McQuillan, A. 2015, MNRAS, 450, 1787

Astropy Collaboration, Price-Whelan, A. M., Sipőcz, B. M., et al. 2018, AJ, 156, 123

Bakos, G. A., Pál, A., Latham, D. W., Noyes, R. W., & Stefanik, R. P. 2006, ApJL, 641, L57

Baraffe, I., Chabrier, G., Barman, T. S., Allard, F., & Hauschildt, P. H. 2003, A&A, 402, 701

Baratella, M., D'Orazi, V., Carraro, G., et al. 2020, A&A, 634, A34

Barnes, S. A., Weingrill, J., Granzer, T., Spada, F., & Strassmeier, K. G. 2015, A&A, 583, A73

Barragán, O., Aigrain, S., Kubyshkina, D., et al. 2019, MNRAS

Berger, T. A., Howard, A. W., & Boesgaard, A. M. 2018, ApJ, 855, 115

Berger, T. A., Huber, D., Gaidos, E., van Saders, J. L., & Weiss, L. M. 2020, arXiv e-prints, 2005

Bhatti, W., Bouma, L., & Yee, S. 2019, cdips-pipeline v0.1.0, https://doi.org/10.5281/zenodo.3370324

Bhatti, W., Bouma, L. G., & Wallace, J. 2018, astrobase, https://doi.org/10.5281/zenodo.1469822

Biddle, L. I., Johns-Krull, C. M., Llama, J., Prato, L., & Skiff, B. A. 2018, ApJL, 853, L34

Bonomo, A. S., Desidera, S., Benatti, S., et al. 2017, A&A, 602, A107

Borucki, W. J., Koch, D., Basri, G., et al. 2010, Science, 327, 977

Bossini, D., Vallenari, A., Bragaglia, A., et al. 2019, A&A, 623, A108

Bouma, L. G., Hartman, J. D., Bhatti, W., Winn, J. N., & Bakos, G. Á. 2019, ApJS, 245, 13

Bouma, L. G., Winn, J. N., Kosiarek, J., & McCullough, P. R. 2017, arXiv:1705.08891 [astro-ph]

Brahm, R., Jordán, A., & Espinoza, N. 2017, PASP, 129, 034002

Brahm, R., Espinoza, N., Jordán, A., et al. 2019, AJ, 158, 45

Brasseur, C. E., Phillip, C., Fleming, S. W., Mullally, S. E., & White, R. L. 2019, Astrophysics Source Code Library, ascl:1905.007

Bravi, L., Zari, E., Sacco, G. G., et al. 2018, A&A, 615, A37

Bressan, A., Marigo, P., Girardi, L., et al. 2012, MNRAS, 427, 127

Brucalassi, A., Koppenhoefer, J., Saglia, R., et al. 2017, A&A, 603, A85

Buchhave, L. A., Bakos, G. A., Hartman, J. D., et al. 2010, ApJ, 720, 1118

Burke, C. J., Gaudi, B. S., DePoy, D. L., & Pogge, R. W. 2006, AJ, 132, 210

Cameron, A. G. W., & Ward, W. R. 1976, 7, Conference Name: Lunar and Planetary Science Conference

Cantat-Gaudin, T., Jordi, C., Vallenari, A., et al. 2018, A&A, 618, A93

Canup, R. M., & Asphaug, E. 2001, Nature, 412, 708

Castelli, F., & Kurucz, R. L. 2004, ArXiv Astrophysics e-prints, astro-ph/0405087

Chatterjee, S., Ford, E. B., Matsumura, S., & Rasio, F. A. 2008, ApJ, 686, 580

Chen, Y., Bressan, A., Girardi, L., et al. 2015, MNRAS, 452, 1068

Chen, Y., Girardi, L., Bressan, A., et al. 2014, MNRAS, 444, 2525

Choi, J., Dotter, A., Conroy, C., et al. 2016, ApJ, 823, 102

Ciardi, D. R., Crossfield, I. J. M., Feinstein, A. D., et al. 2018, AJ, 155, 10

Claret, A. 2017, A&A, 600, A30

Collins, K. A., Kielkopf, J. F., Stassun, K. G., & Hessman, F. V. 2017, AJ, 153, 77

Cropper, M., Katz, D., Sartoretti, P., et al. 2018, A&A, 616, A5

Crouzet, N., Chapellier, E., Guillot, T., et al. 2018, A&A, 619, A116

Curtis, J. L., Agüeros, M. A., Douglas, S. T., & Meibom, S. 2019a, ApJ, 879, 49

Curtis, J. L., Agüeros, M. A., Mamajek, E. E., Wright, J. T., & Cummings, J. D. 2019b, AJ, 158, 77

Daban, J.-B., Gouvret, C., Guillot, T., et al. 2010, 7733, 77334T

Damasso, M., Lanza, A. F., Benatti, S., et al. 2020, arXiv e-prints, 2008, arXiv:2008.09445

Damiani, F., Prisinzano, L., Pillitteri, I., Micela, G., & Sciortino, S. 2019, A&A, 623, A112, publisher: EDP Sciences

Dauphas, N., & Pourmand, A. 2011, Nature, 473, 489

David, T., Hillenbrand, L., & Petigura, E. 2016, Nature, 534, 658

David, T. J., & Hillenbrand, L. A. 2015, ApJ, 804, 146

David, T. J., Petigura, E. A., Luger, R., et al. 2019a, ApJL, 885, L12

David, T. J., Mamajek, E. E., Vanderburg, A., et al. 2018, AJ, 156, 302

David, T. J., Cody, A. M., Hedges, C. L., et al. 2019b, AJ, 158, 79

de Zeeuw, P. T., Hoogerwerf, R., de Bruijne, J. H. J., Brown, A. G. A., & Blaauw, A. 1999, AJ, 117, 354

Díaz, R. F., Almenara, J. M., Santerne, A., et al. 2014, MNRAS, 441, 983

Dobbie, P. D., Lodieu, N., & Sharp, R. G. 2010, MNRAS, 409, 1002

Donati, J.-F., Semel, M., Carter, B. D., Rees, D. E., & Collier Cameron, A. 1997, MNRAS, 291, 658

Donati, J. F., Moutou, C., Malo, L., et al. 2016, Nature, advance online publication

Donati, J.-F., Bouvier, J., Alencar, S. H., et al. 2020, MNRAS, 491, 5660

Dotter, A. 2016, ApJS, 222, 8

Douglas, S. T., Agüeros, M. A., Covey, K. R., & Kraus, A. 2017, ApJ, 842, 83

Douglas, S. T., Curtis, J. L., Agüeros, M. A., et al. 2019, ApJ, 879, 100

Dullemond, C. P., & Monnier, J. D. 2010, ARA&A, 48, 205

Eastman, J., Siverd, R., & Gaudi, B. S. 2010, PASP, 122, 935

Ekström, S., Georgy, C., Eggenberger, P., et al. 2012, A&A, 537, A146

Evans, D. W., Riello, M., De Angeli, F., et al. 2018, A&A, 616, A4

Fabrycky, D., & Tremaine, S. 2007, ApJ, 669, 1298

Fedele, D., van den Ancker, M. E., Henning, T., Jayawardhana, R., & Oliveira, J. M. 2010, A&A, 510, A72

Feiden, G. A., & Chaboyer, B. 2013, ApJ, 779, 183

Fűrész, G., Szentgyorgyi, A. H., & Meibom, S. 2008, 287

Flagg, L., Johns-Krull, C. M., Nofi, L., et al. 2019, ApJ, 878, L37

Foreman-Mackey, D. 2016, Journal of Open Source Software, 1, 24

Foreman-Mackey, D., Czekala, I., Luger, R., et al. 2020, exoplanet-dev/exoplanet v0.2.6

Fortney, J. J., Marley, M. S., & Barnes, J. W. 2007, ApJ, 659, 1661

Fulton, B. J., Petigura, E. A., Blunt, S., & Sinukoff, E. 2018, PASP, 130, 044504

Fulton, B. J., Petigura, E. A., Howard, A. W., et al. 2017, AJ, 154, 109

Gaia Collaboration, Prusti, T., de Bruijne, J. H. J., et al. 2016, A&A, 595, A1

Gaia Collaboration, Brown, A. G. A., Vallenari, A., et al. 2018, A&A, 616, A1

Gaudi, B. S., & Winn, J. N. 2007, ApJ, 655, 550

Gelman, A., & Rubin, D. B. 1992, Statistical Science, 7, 457, publisher: Institute of Mathematical Statistics

Giacalone, S., & Dressing, C. D. 2020, arXiv e-prints, arXiv:2002.00691

Gilbert, J., Bergmann, C., Bloxham, G., et al. 2018, 0702, 107020Y, Conference Name: Ground-based and Airborne Instrumentation for Astronomy VII ISBN: 9781510619579 arXiv:1807.01938

Ginsburg, A., Sipocz, B., Madhura Parikh, et al. 2018, Astropy/Astroquery: V0.3.7 Release

Ginzburg, S., Schlichting, H. E., & Sari, R. 2016, ApJ, 825, 29

Girardi, L., Groenewegen, M. A. T., Hatziminaoglou, E., & da Costa, L. 2005, A&A, 436, 895

Gray, D. F. 2005, The Observation and Analysis of Stellar Photospheres

Gray, R. O., & Corbally, C. J. 1994, AJ, 107, 742

Gupta, A., & Schlichting, H. E. 2019, MNRAS, 487, 24

—. 2020, MNRAS, 493, 792

Hartman, J. D., Gaudi, B. S., Holman, M. J., et al. 2009, ApJ, 695, 336

Hippke, M., David, T. J., Mulders, G. D., & Heller, R. 2019, arXiv:1906.00966 [astro-ph]

Hirano, T., Krishnamurthy, V., Gaidos, E., et al. 2020, arXiv:2006.13243 [astro-ph]

Hoffman, M. D., & Gelman, A. 2014, Journal of Machine Learning Research, 15, 1593

Howard, A. W., Marcy, G. W., Bryson, S. T., et al. 2012, ApJS, 201, 15

Howell, S. B., Sobeck, C., Haas, M., et al. 2014, PASP, 126, 398

Huang, C. X., Shporer, A., Dragomir, D., et al. 2018a, arXiv:1807.11129 [astro-ph]

Huang, C. X., Burt, J., Vanderburg, A., et al. 2018b, ApJ, 868, L39

Hunter, J. D. 2007, Computing in Science & Engineering, 9, 90

Irwin, J., & Bouvier, J. 2009, in , eprint: arXiv:0901.3342, 363

Irwin, J., Irwin, M., Aigrain, S., et al. 2007, MNRAS, 375, 1449

Jenkins, J. M., Twicken, J. D., McCauliff, S., et al. 2016, Software and Cyberinfrastructure for Astronomy IV, 9913, 99133E

Jensen, E. 2013, Tapir: A web interface for transit/eclipse observability, Astrophysics Source Code Library, ascl:1306.007

Johns-Krull, C. M., McLane, J. N., Prato, L., et al. 2016, ApJ, 826, 206

Jones, E., Oliphant, T., Peterson, P., et al. 2001, Open source scientific tools for Python

Jordán, A., Brahm, R., Espinoza, N., et al. 2020, AJ, 159, 145

Kaufer, A., Stahl, O., Tubbesing, S., et al. 1999, The Messenger, 95, 8

Kharchenko, N. V., Piskunov, A. E., Röser, S., Schilbach, E., & Scholz, R.-D. 2005, A&A, 438, 1163

Kharchenko, N. V., Piskunov, A. E., Schilbach, E., Röser, S., & Scholz, R.-D. 2013, A&A, 558, A53

King, G. W., & Wheatley, P. J. 2020, arXiv:2007.13731 [astro-ph]

Kipping, D. M. 2013, MNRAS, 435, 2152

Kleine, T., Touboul, M., Bourdon, B., et al. 2009, Geochimica et Cosmochimica Acta, 73, 5150

König, S., Münker, C., Hohl, S., et al. 2011, Geochimica et Cosmochimica Acta, 75, 2119

Kounkel, M., & Covey, K. 2019, AJ, 158, 122

Krumholz, M. R., McKee, C. F., & Bland-Hawthorn, J. 2019, ARA&A, 57, 227

Kumar, R., Carroll, C., Hartikainen, A., & Martin, O. A. 2019, The Journal of Open Source Software

Kurucz, R. L. 2013, Astrophysics Source Code Library, ascl:1303.024

Lada, C. J., & Lada, E. A. 2003, ARA&A, 41, 57

Landsman, W. B. 1995, in Astronomical Society of the Pacific Conference Series, Vol. 77, Astronomical Data Analysis Software and Systems IV, ed. R. A. Shaw, H. E. Payne, & J. J. E. Hayes, 437

Li, J., Tenenbaum, P., Twicken, J. D., et al. 2019, PASP, 131, 024506

Lightkurve Collaboration, Cardoso, J. V. d. M., Hedges, C., et al. 2018, Lightkurve: Kepler and TESS time series analysis in Python, Astrophysics Source Code Library, ascl:1812.013

Lin, D. N. C., Bodenheimer, P., & Richardson, D. C. 1996, Nature, 380, 606

Lindegren, L., Hernández, J., Bombrun, A., et al. 2018, A&A, 616, A2

Lithwick, Y., & Wu, Y. 2014, Proceedings of the National Academy of Sciences, 111, 12610

Livingston, J. H., Dai, F., Hirano, T., et al. 2018, AJ, 155, 115

—. 2019, MNRAS, 484, 8

Lomb, N. R. 1976, Astrophysics and Space Science, 39, 447

Lovis, C., & Mayor, M. 2007, A&A, 472, 657

Luger, R., Agol, E., Foreman-Mackey, D., et al. 2019, AJ, 157, 64

Malavolta, L., Nascimbeni, V., Piotto, G., et al. 2016, A&A, 588, A118

Mamajek, E. E. 2009, 1158, 3, Conference Name: Exoplanets and Disks: Their Formation and Diversity Place: eprint: arXiv:0906.5011

Mamajek, E. E., & Hillenbrand, L. A. 2008, ApJ, 687, 1264

Mann, A. W., Gaidos, E., & Ansdell, M. 2013, ApJ, 779, 188

Mann, A. W., Gaidos, E., Mace, G. N., et al. 2016a, ApJ, 818

Mann, A. W., Newton, E. R., Rizzuto, A. C., et al. 2016b, AJ, 152, 61

Mann, A. W., Gaidos, E., Vanderburg, A., et al. 2017, AJ, 153, 64

Mann, A. W., Vanderburg, A., Rizzuto, A. C., et al. 2018, AJ, 155, 4

Mann, A. W., Johnson, M. C., Vanderburg, A., et al. 2020, arXiv:2005.00047 [astro-ph]

Mansfield, M., Bean, J. L., Oklopčić, A., et al. 2018, ApJ, 868, L34

Marigo, P., Girardi, L., Bressan, A., et al. 2017, ApJ, 835, 77

Martioli, E., Hebrard, G., Moutou, C., et al. 2020, arXiv:2006.13269 [astro-ph]

Mayor, M., Marmier, M., Lovis, C., et al. 2011, ArXiv e-prints, 1109, arXiv:1109.2497

McKinney, W. 2010, in Proceedings of the 9th Python in Science Conference, ed. S. van der Walt & J. Millman, 51

Meibom, S., Barnes, S. A., Platais, I., et al. 2015, Nature, 517, 589

Meibom, S., Torres, G., Fressin, F., et al. 2013, Nature, 499, 55

Mékarnia, D., Guillot, T., Rivet, J.-P., et al. 2016, MNRAS, 463, 45

Mermilliod, J. C. 1981, A&A, 97, 235

Miller, A. A., Irwin, J., Aigrain, S., Hodgkin, S., & Hebb, L. 2008, MNRAS, 387, 349

Mochejska, B. J., Stanek, K. Z., Sasselov, D. D., et al. 2005, AJ, 129, 2856

—. 2006, AJ, 131, 1090

Montet, B. T., Feinstein, A. D., Luger, R., et al. 2020, AJ, 159, 112

Morbidelli, A., Lunine, J. I., O'Brien, D. P., Raymond, S. N., & Walsh, K. J. 2012, Annual Review of Earth and Planetary Sciences, 40, 251

Morton, T. D. 2012, ApJ, 761, 6

Morton, T. D. 2015a, isochrones: Stellar model grid package

—. 2015b, VESPA: False positive probabilities calculator, Astrophysics Source Code Library, ascl:1503.011

Morton, T. D., Bryson, S. T., Coughlin, J. L., et al. 2016, ApJ, 822, 86

Nardiello, D., Piotto, G., Deleuil, M., et al. 2020, MNRAS, 495, 4924

Netopil, M., Paunzen, E., Heiter, U., & Soubiran, C. 2016, A&A, 585, A150

Newton, E. R., Mann, A. W., Tofflemire, B. M., et al. 2019, ApJ, 880, L17

Obermeier, C., Henning, T., Schlieder, J. E., et al. 2016, AJ, 152, 223

Oh, S., Price-Whelan, A. M., Hogg, D. W., Morton, T. D., & Spergel, D. N. 2017, AJ, 153, 257

Oklopčić, A., & Hirata, C. M. 2018, ApJL, 855, L11

Owen, J. E., & Wu, Y. 2013, ApJ, 775, 105

—. 2017, ApJ, 847, 29

Palle, E., Oshagh, M., Casasayas-Barris, N., et al. 2020, arXiv:2006.13609 [astro-ph]

Paxton, B., Bildsten, L., Dotter, A., et al. 2011, ApJS, 192, 3

Paxton, B., Cantiello, M., Arras, P., et al. 2013, ApJS, 208, 4

Paxton, B., Marchant, P., Schwab, J., et al. 2015, ApJS, 220, 15

Pepper, J., Stanek, K. Z., Pogge, R. W., et al. 2008, AJ, 135, 907

Pérez, F., & Granger, B. E. 2007, Computing in Science and Engineering, 9, 21

Petigura, E. A., Marcy, G. W., Winn, J. N., et al. 2018, AJ, 155, 89

Plavchan, P., Barclay, T., Gagné, J., et al. 2020, Nature, 582, 497

Pollack, J. B., Hubickyj, O., Bodenheimer, P., et al. 1996, Icarus, 124, 62

Quinn, S. N., White, R. J., Latham, D. W., et al. 2012, ApJL, 756, L33

Raghavan, D., McAlister, H. A., Henry, T. J., et al. 2010, ApJS, 190, 1

Rajpaul, V., Aigrain, S., Osborne, M. A., Reece, S., & Roberts, S. 2015, MNRAS, 452, 2269

Rajpurohit, A. S., Reylé, C., Allard, F., et al. 2013, A&A, 556, A15

Randich, S., Tognelli, E., Jackson, R., et al. 2018, A&A, 612, A99

Raymond, S. N., Kokubo, E., Morbidelli, A., Morishima, R., & Walsh, K. J. 2014, Protostars and Planets VI, 595

Rebull, L. M., Stauffer, J. R., Cody, A. M., et al. 2020

Rebull, L. M., Stauffer, J. R., Bouvier, J., et al. 2016, AJ, 152, 113

Ricker, G. R., Winn, J. N., Vanderspek, R., et al. 2015, Journal of Astronomical Telescopes, Instruments, and Systems, 1, 014003

Rizzuto, A. C., Vanderburg, A., Mann, A. W., et al. 2018, AJ, 156, 195

Rizzuto, A. C., Newton, E. R., Mann, A. W., et al. 2020, arXiv:2005.00013 [astro-ph]

Rohatgi, A. 2019, WebPlotDigitizer: v4.2

Salvatier, J., Wieckiâ, T. V., & Fonnesbeck, C. 2016, PyMC3: Python probabilistic programming framework

Sanchis-Ojeda, R., Winn, J. N., Marcy, G. W., et al. 2013, The Astrophysical Journal, 775, 54

Santerne, A., Díaz, R. F., Almenara, J.-M., et al. 2015, MNRAS, 451, 2337

Sato, B., Izumiura, H., Toyota, E., et al. 2007, ApJ, 661, 527

Scargle, J. D. 1982, ApJ, 263, 835

Seager, S., & Mallén-Ornelas, G. 2003, ApJ, 585, 1038

Servén, D., Brummitt, C., & Abedi, H. 2018, dswah/pyGAM: v0.8.0

Skrutskie, M. F., Cutri, R. M., Stiening, R., et al. 2006, AJ, 131, 1163

Skumanich, A. 1972, ApJ, 171, 565

Smith, J. C., Morris, R. L., Jenkins, J. M., et al. 2016, PASP, 128, 124501

Smith, J. C., Stumpe, M. C., Cleve, J. E. V., et al. 2012, PASP, 124, 1000

Soderblom, D. R. 2010, ARA&A, 48, 581

Soderblom, D. R., Hillenbrand, L. A., Jeffries, R. D., Mamajek, E. E., & Naylor, T. 2014, Protostars and Planets VI, 219

Spake, J. J., Sing, D. K., Evans, T. M., et al. 2018, Nature, 557, 68

Stassun, K. G., Collins, K. A., & Gaudi, B. S. 2017, AJ, 153, 136

Stassun, K. G., Oelkers, R. J., Pepper, J., et al. 2018, AJ, 156, 102

Stassun, K. G., Oelkers, R. J., Paegert, M., et al. 2019, arXiv:1905.10694 [astro-ph]

Stauffer, J. R., Hartmann, L. W., Prosser, C. F., et al. 1997, ApJ, 479, 776

Stauffer, J. R., Jones, B. F., Backman, D., et al. 2003, AJ, 126, 833

Stumpe, M. C., Smith, J. C., Catanzarite, J. H., et al. 2014, PASP, 126, 100

Sullivan, P. W., et al. 2015, ApJ, 809, 77

Theano Development Team. 2016, arXiv e-prints, abs/1605.02688

Tokovinin, A. 2018, PASP, 130, 035002

Tokovinin, A., Fischer, D. A., Bonati, M., et al. 2013, PASP, 125, 1336

Torres, G., Fressin, F., Batalha, N. M., et al. 2011, ApJ, 727, 24

Touboul, M., Kleine, T., Bourdon, B., Palme, H., & Wieler, R. 2007, Nature, 450, 1206

Twicken, J. D., Catanzarite, J. H., Clarke, B. D., et al. 2018, PASP, 130, 064502

van Leeuwen, F. 2009, A&A, 497, 209

Vanderburg, A., Mann, A. W., Rizzuto, A., et al. 2018, AJ, 156, 46

Vanderburg, A., Huang, C. X., Rodriguez, J. E., et al. 2019, ApJ, 881, L19

VanderPlas, J. T., & Ivezić, Z. 2015, ApJ, 812, 18

Žerjal, M., Zwitter, T., Matijevič, G., et al. 2017, ApJ, 835, 61

Žerjal, M., Ireland, M. J., Nordlander, T., et al. 2019, MNRAS, 484, 4591

Walt, S. v. d., Colbert, S. C., & Varoquaux, G. 2011, Computing in Science & Engineering, 13, 22

Weber, E. J., & Davis, Jr., L. 1967, ApJ, 148, 217

Williams, J. P., & Cieza, L. A. 2011, ARA&A, 49, 67

Wright, E. L., Eisenhardt, P. R. M., Mainzer, A. K., et al. 2010, AJ, 140, 1868

Wright, J. T., Marcy, G. W., Howard, A. W., et al. 2012, ApJ, 753, 160

Yu, L., Donati, J.-F., Hébrard, E. M., et al. 2017, MNRAS, 467, 1342

Zahn, J.-P. 1977, A&A, 500, 121

Zhou, G., Rodriguez, J. E., Vanderburg, A., et al. 2018, AJ, 156, 93

Zhou, G., Winn, J. N., Newton, E. R., et al. 2020, The Astrophysical Journal, 892, L21

Ziegler, C., Tokovinin, A., Briceño, C., et al. 2020, AJ, 159, 19

Zuckerman, B., & Song, I. 2004, ARA&A, 42, 685